ANDREW HYNES SERIES: TECTONIC PROCESSES

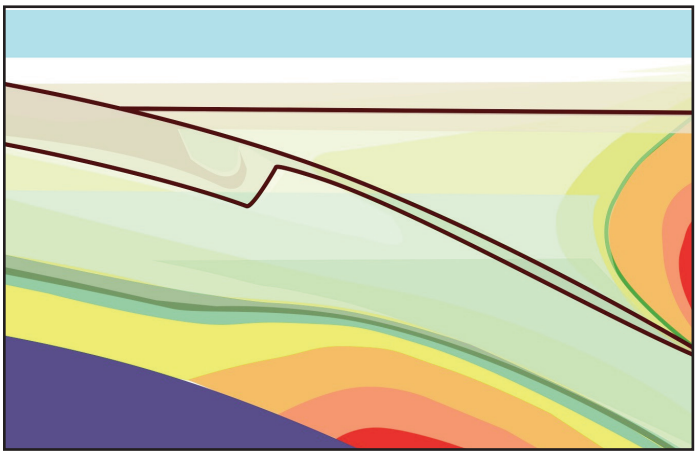

Neoarchean Mantle-derived Magmatism within the Repulse Bay Block, Melville Peninsula, Nunavut: Implications for Archean Crustal Extraction and Cratonization

Crystal LaFlamme[1*], Christopher R.M. McFarlane[1], David Corrigan[2]

[1]Department of Earth Sciences,
University of New Brunswick,
2 Bailey Drive, Fredericton, NB, E3B 5A, Canada

[*]Centre for Exploration Targeting
University of Western Australia
35 Stirling Hwy, Crawley, WA 6009, Australia
Email: crystal.laflamme@uwa.edu.au

[2]Geological Survey of Canada,
601 Booth Street,
Ottawa, Ontario, K1A 0E8, Canada

SUMMARY

The Repulse Bay block (RBb) of the southern Melville Peninsula, Nunavut, lies within the Rae craton and exposes a large (50,000 km^2) area of middle to lower crust. The block is composed of ca. 2.86 Ga and 2.73–2.71 Ga tonalite-trondhjemite-granodiorite (TTG) and granitic gneiss that was derived from an older 3.25 and 3.10 Ga crustal substrate. This period of crustal generation was followed by the emplacement of ca. 2.69–2.66 Ga enderbite, charnockite, and granitoid intrusions with entrained websterite xenoliths. These voluminous batholith-scale bodies (dehydrated and hydrated intrusions), and the associated websterite xenoliths, have similar whole rock geochemical properties, including fractionated light rare earth element (LREE)–heavy (H)REE whole rock patterns and negative Nb, Ti, and Ta anomalies. Dehydrated intrusions and websterite xenoliths also contain similar mineralogy (two pyroxene, biotite, interstitial amphibole) and similar pyroxene trace element compositions. Based on geochemical and mineralogical properties, the two lithologies are interpreted to be related by fractional crystallization, and to be the product of a magmatic cumulate processes. Reworking of the crust in a ca. 2.72 Ga subduction zone setting was followed by ca. 2.69 Ga upwelling of the asthenospheric mantle and the intrusion of massif-type granitoid plutons. Based on a dramatic increase in FeO, Zr, Hf, and LREE content of the most evolved granitoid components from the 2.69–2.66 Ga cumulate intrusion, we propose that those granitoid plutons were in part derived from a metasomatized mantle source enriched by fluids from the subducting oceanic slab that underwent further hybridization (via assimilation) with the crust. Large-scale, mantle-derived Neoarchean sanukitoid-type magmatism played a role in the development of a depleted lower crust and residual sub-continental lithospheric mantle, a crucial element in the preservation of the RBb.

RÉSUMÉ

Le bloc de Repulse Bay (RBb) dans le sud de la péninsule de Melville, au Nunavut, est situé dans le craton de Rae et expose une large zone (50 000 km^2) de croûte moyenne à inférieur. Ce bloc est composé de tonalite-trondhjémite-granodiorite (TTG) daté à ca. 2,86 Ga et 2,73–2,71 Ga, et de gneiss granitique dérivé d'un substrat crustal plus ancien daté à 3,25 Ga et 3,10 Ga. Cette période de croissance crustale a été suivie par la mise en place entre ca. 2,69 et 2,66 Ga d'intrusions d'enderbite, charnockite et de granitoïde incluant des xénolites d'entraînement de websterite. Ces intrusions de taille batholitique (intrusions déshydratées et hydratées) ainsi que les xénolites d'entraînement de websterite associés, ont des propriétés géochimiques sur roche totale semblables notamment leurs profils de fractionnement des terres rares légers (*LREE*) et des terres

rares lourds (*HREE)* ainsi que leurs anomalies négatives en Nb, Ti et Ta. Les intrusions déshydratées et les xénolites de websterite ont aussi des minéralogies similaires (deux pyroxènes, biotite, amphibole interstitielle) ainsi que des compositions semblables en éléments traces de leurs pyroxènes. Étant donné leurs propriétés géochimiques et minéralogiques, ces deux lithologies sont interprétées comme provenant d'une cristallisation fractionnée, et comme étant le produit de processus d'accumulations magmatiques. Le remaniement de la croûte dans un contexte de subduction vers ca. 2,72 Ga, a été suivi vers ca. 2,69 Ga d'une remontée du manteau asthénosphérique et de l'intrusion de granitoïdes de type massif. D'après l'importante augmentation en FeO, Zr, Hf et *LREE* dans les granitoïdes les plus évolués du magmatisme ayant pris place entre ca. 2,69 Ga et 2,66 Ga, nous proposons que ces plutons aient été en partie dérivés d'une source mantélique métasomatisée enrichies par des fluides d'une plaque océanique en subduction et qui a subi une hybridation supplémentaire (par assimilation) avec la croûte. Le magmatisme néoarchéen de type sanukitoïde, dérivé du manteau et de grande échelle, a joué un rôle dans le développement d'une croûte inférieure et d'un manteau lithosphérique continental résiduel appauvri, un élément déterminant pour la préservation du RBb.

Traduit par le Traducteur

INTRODUCTION

The Neoarchean is a discernible era in the formation, evolution and stabilization of large volumes of continental crust (Moyen et al. 2001; Martin and Moyen 2002; Halla et al. 2009; Hawkesworth et al. 2010; Rapp et al. 2010; Laurent et al. 2011; Heilimo et al. 2013). This time period represents a transition to the generation of moderate to high pressure tonalite-trondhjemite-granodiorite (TTG), sanukitoid rocks, and high-K granite (e.g. Shirey and Hanson 1984; Smithies and Champion 2000; Martin et al. 2005; Halla et al. 2009; Rapp et al. 2010; Laurent et al. 2014) and the final stability of Archean cratons that had previously undergone rapid recycling (Hawkesworth et al. 2010). The sanukitoid suite is composed of Neoarchean granitoid lithologies that contain both an 'arc-like' and 'mantle-like' signatures that reflect their generation from a mantle peridotite source, rich in incompatible elements (Stern et al. 1989; Laurent et al. 2014 and references therein). Numerous studies have highlighted the similarities in geochemical characteristics of Neoarchean TTG-type gneiss, sanukitoid rocks and high-K granite (e.g. Smithies and Champion 2000; Martin et al. 2005, 2010; Halla et al. 2009; Rapp et al. 2010) that preserve a mantle affinity (high MgO, Mg #, Ni, Cr, Co, V, etc.) and 'arc-like' signatures (Nb, Ta and Ti troughs, enrichment in LILE and LREE) generally derived from slab melts (Martin and Moyen 2002; Halla 2005; Halla et al. 2009).

High grade, Neoarchean granulite terranes have been observed worldwide and are locally exposed in the northern Superior craton (e.g. Davis et al. 2005; Boily et al. 2009; Heaman et al. 2011). Granulite terranes can preserve regional scale, pyroxene-bearing, massif-type calc-alkalic intrusions (Fyfe 1973; Rudnick and Fountain 1995). Similar to sanukitoid intrusions, these charnockitic intrusions preserve geochemical trace element patterns typical of Neoarchean TTGs and modern day arc environments (Percival and Mortensen 2002). The generation of Neoarchean charnockite intrusions occurred in a period that recorded a fundamental break in Archean crustal evolution worldwide: the cessation of greenstone belt and TTG formation (e.g. Heaman et al. 2011). These hot, CO_2-laden charnockite intrusions (containing igneous ortho- and clinopyroxene) have been described as the driving force for the formation of granulite terranes during their emplacement (Frost and Frost 2008) and may be critical in Neoarchean crust stabilization.

North of the aforementioned northern Superior craton lies the Repulse Bay block (RBb), interpreted to represent (in part) a lower crustal (granulitic) section of the Rae craton that was exhumed during the Paleoproterozoic Trans-Hudson orogeny (LaFlamme et al. 2014b). The Archean crust of the RBb records a number of crustal formation and reworking events including the generation of ca. 2.86 Ga and ca. 2.73–2.71 Ga biotite ± hornblende TTG-type gneiss and sheets of diorite, and ca. 2.69–2.66 Ga biotite–hornblende ± clinopyroxene granitoid rocks and orthopyroxene–clinopyroxene–biotite–hornblende charnockite and enderbite intrusions containing ultramafic xenoliths (LaFlamme et al. 2014a, b). The goal of this paper is to investigate the petrogenesis of these Neoarchean high grade rocks. By investigating the geochemical signature and pressure (*P*)–temperature (*T*) conditions of their formation, we can determine the geodynamic setting in which a regional scale massif-type charnockite suite was generated and speculate on the role anhydrous plutonism had in the stabilization of the continental crust and subsequent preservation of the RBb. Because the RBb is interpreted to be a slice of deeply exhumed Rae craton (LaFlamme et al. 2014b), it serves as a window into the mid-crustal processes presumed to have occurred regionally during cratonization of the Rae Province. This paper seeks to utilize new whole rock and mineral chemical data presented here, in addition to the geological, geochronological, and isotopic framework presented by LaFlamme et al. (2014a) and LaFlamme et al. (2014b), to specifically characterize Neoarchean crustal formation.

REGIONAL GEOLOGY

The Western Churchill Province (WCP) is composed of the Archean granite–greenstone belts and high grade equivalents, and Paleoproterozoic supracrustal sequences and intrusions that underwent numerous tectonothermal episodes (Fig. 1; Berman 2010 and references therein). The north–central segment of the Western Churchill Province is divided into two main crustal divisions, the Rae and Hearne cratons (Hoffman 1988). The Rae craton is made up of Mesoarchean to Neoarchean north-northwesterly trending granite–greenstone belts composed of komatiite, mafic and felsic volcanic rocks, conglomerate, quartzite, pelite, and iron formations (Frisch 2000; Zaleski et al. 2001; Bethune and Scammell 2003; Skulski et al. 2003; Corrigan et al. 2013). Rare Mesoarchean to Neoarchean calc-alkalic gneiss complexes are sandwiched between the low grade belts (Zaleski et al. 2001; Hartlaub et al. 2005; Rayner et al. 2013). Intruded into the granite–greenstone belts and their high-grade equivalent gneiss complexes are ca. 2.73–2.67 Ga calc-alkaline, felsic to intermediate plutonic suites and gneiss (Bethune and Scammell 2003; van Breemen et al. 2007; Rayner et al. 2011; Hinchey et al. 2011).

Based on evidence for a polycyclic tectonic history, exten-

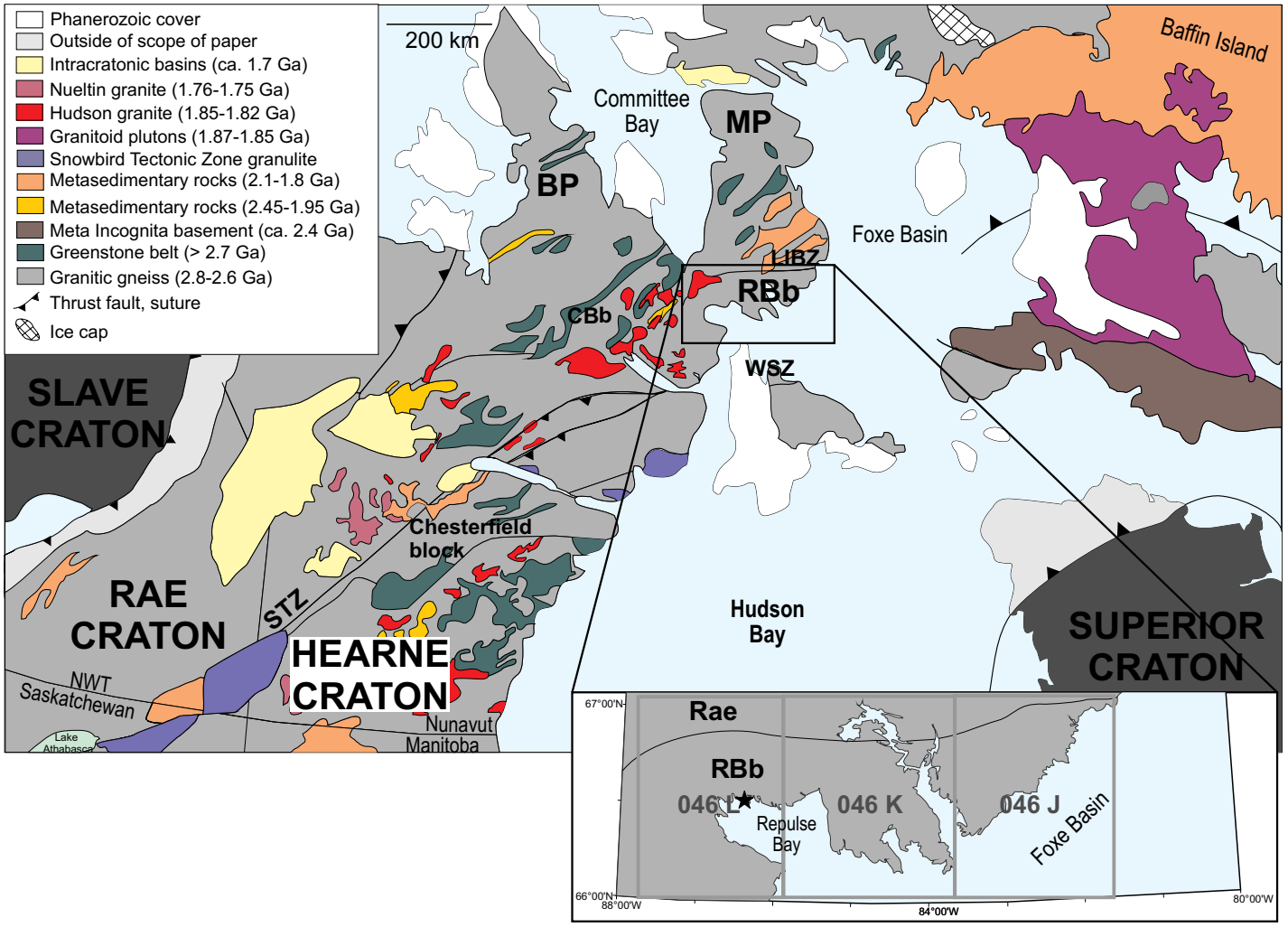

Figure 1. General geology of the western Churchill Province and surrounding area showing the location of the studied area of the Repulse Bay block, Melville Peninsula, Nunavut. Regional scale geology modified from Berman et al. (2005) and references therein. Abbreviations: BP, Boothia Peninsula; CBb, Chesterfield block; LIBZ, Lyon Inlet Boundary Zone; MP, Melville Peninsula; RBb, Repulse Bay block; STZ, Snowbird Tectonic Zone. The study area of the RBb is enclosed by the black box. 1:250,000-scale NTS map sheet 046J, 046K, 046L are overlain on the map as grey boxes. Black star denotes the hamlet of Repulse Bay.

sive plutonism, and distinct mafic dyke swarms, Davis et al. (2006) demonstrated that the Chesterfield block (previously the northwest Hearne subdomain) was accreted to the Rae craton at 2.64–2.61 Ga. The collision between the two cratons resulted in Archean tectonometamorphism at ca. 2.66 Ga and ca. 2.55 Ga (Davis et al. 2006). Collision was followed by 2.62–2.58 Ga 'I-type' dominantly monzogranitic plutonism (Skulski et al. 2003; Davis et al. 2006; van Breemen et al. 2007; Rayner et al. 2011) that has been described in areas as 'high-K' (Hinchey et al. 2011).

LOCAL GEOLOGY

The RBb high grade gneiss complex lies within the Rae craton and occurs at the southern end of the Melville Peninsula, Nunavut. The block is bounded to the north by the Lyon Inlet boundary zone and is interpreted to extend southwards to the Wager shear zone and westwards towards the Committee Bay belt (Fig. 1; see LaFlamme et al. 2014b). The lithologies comprising the block include: 1) ca. 2.86 Ga and 2.73–2.71 Ga granitoid gneiss and metadiorite sheets, 2) ca. 2.69–2.66 Ga charnockite to enderbite and dominantly monzogranitic plutons, and 3) < 1.89 Ga pelite–marble sequences occurring as slivers between tectonized granitoid sheets (LaFlamme et al. 2014b). Lithologies of the RBb are uniformly subhorizontal and undulating. The strike of the units is dominantly east–west and curves to the northeast–southwest in the extreme western portion of the mapped area. The RBb is separated into two segments by the Qaggitalik shear zone; the eastern–central portion of the RBb preserves a deeper (granulite facies) segment of crust than the shallower (upper amphibolite to lower granulite facies) western portion (LaFlamme et al. 2014b). A geological map initially prepared at 1:2,000,000 scale of the study area of the RBb with sample locations is presented in Figure 2.

Archean TTG Protoliths

Granitoid gneiss of the RBb are composed of ca. 2.86 and 2.73 Ga biotite–hornblende tonalite, granodiorite, monzodiorite, monzogranite, and minor trondhjemite gneiss. This unit is heterogeneous and medium- to coarse-grained, and occurs as a moderate to low (green) signal in the combined aeromagnetic and total eU radiometric map (Fig. 3). The gneissic fabric is

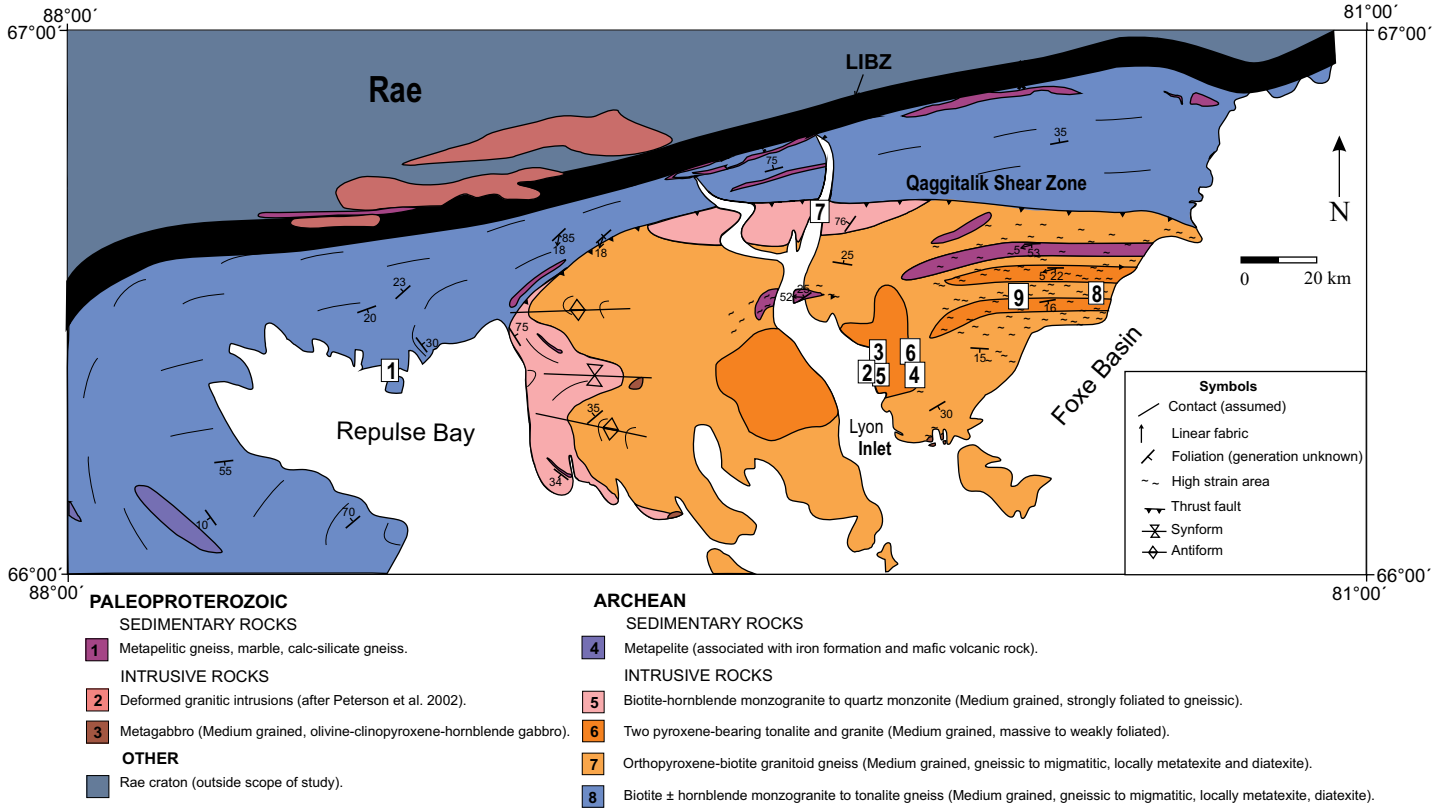

Figure 2. Geological map that denoted metamorphic domains of the study area of the Repulse Bay block (units 1 through 8; block extends to the south and west). Modified with sample locations after LaFlamme et al. (2014b). LIBZ – Lyon Inlet Boundary Zone.

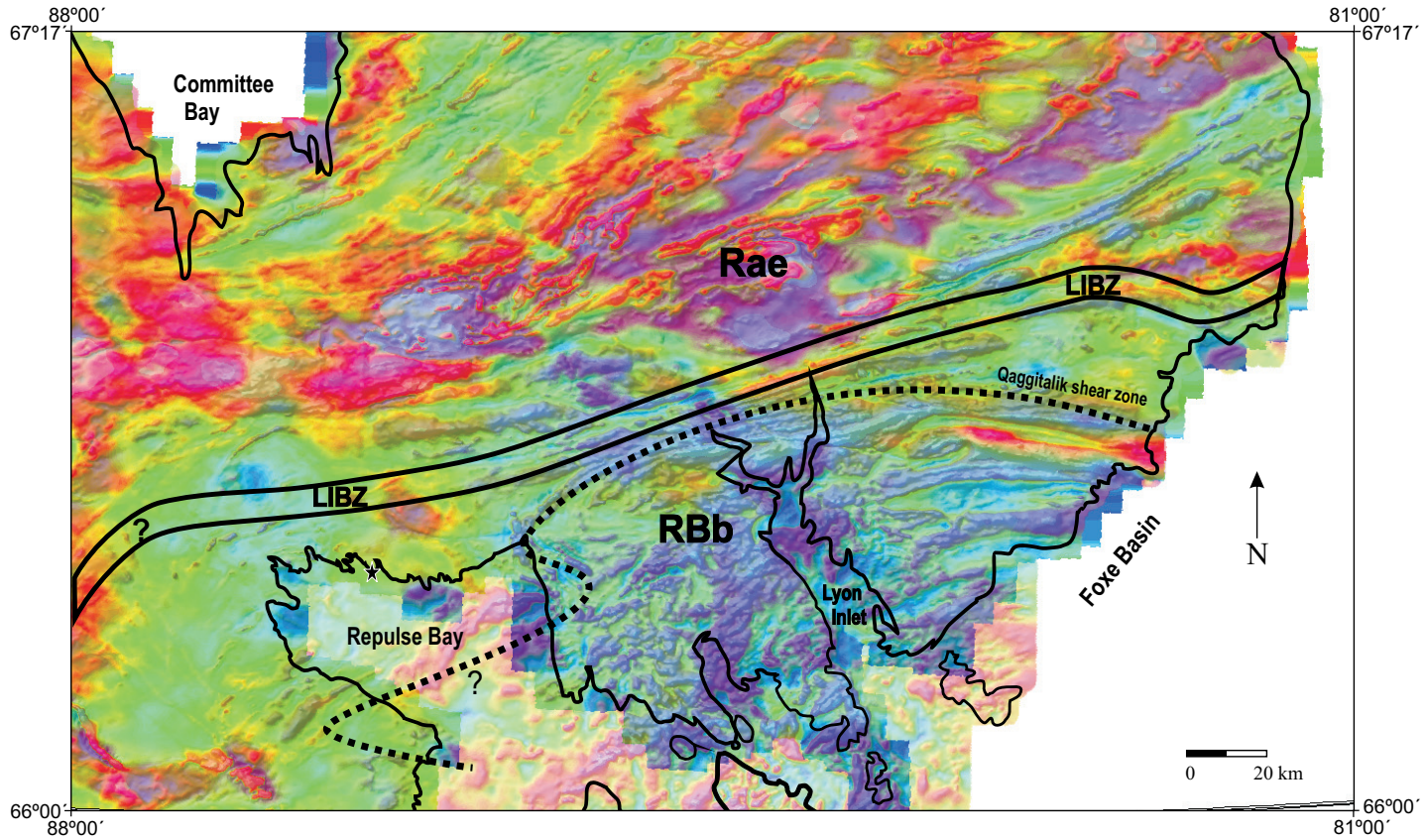

Figure 3. Combined airborne magnetic map and airborne radiometric map (equivalent U (eU); 800 m spacing) of the Repulse Bay block (RBb). Anomalously high magnetic properties in red and low in blue. High total U is in red, and low in blue. LIBZ – Lyon Inlet Boundary Zone.

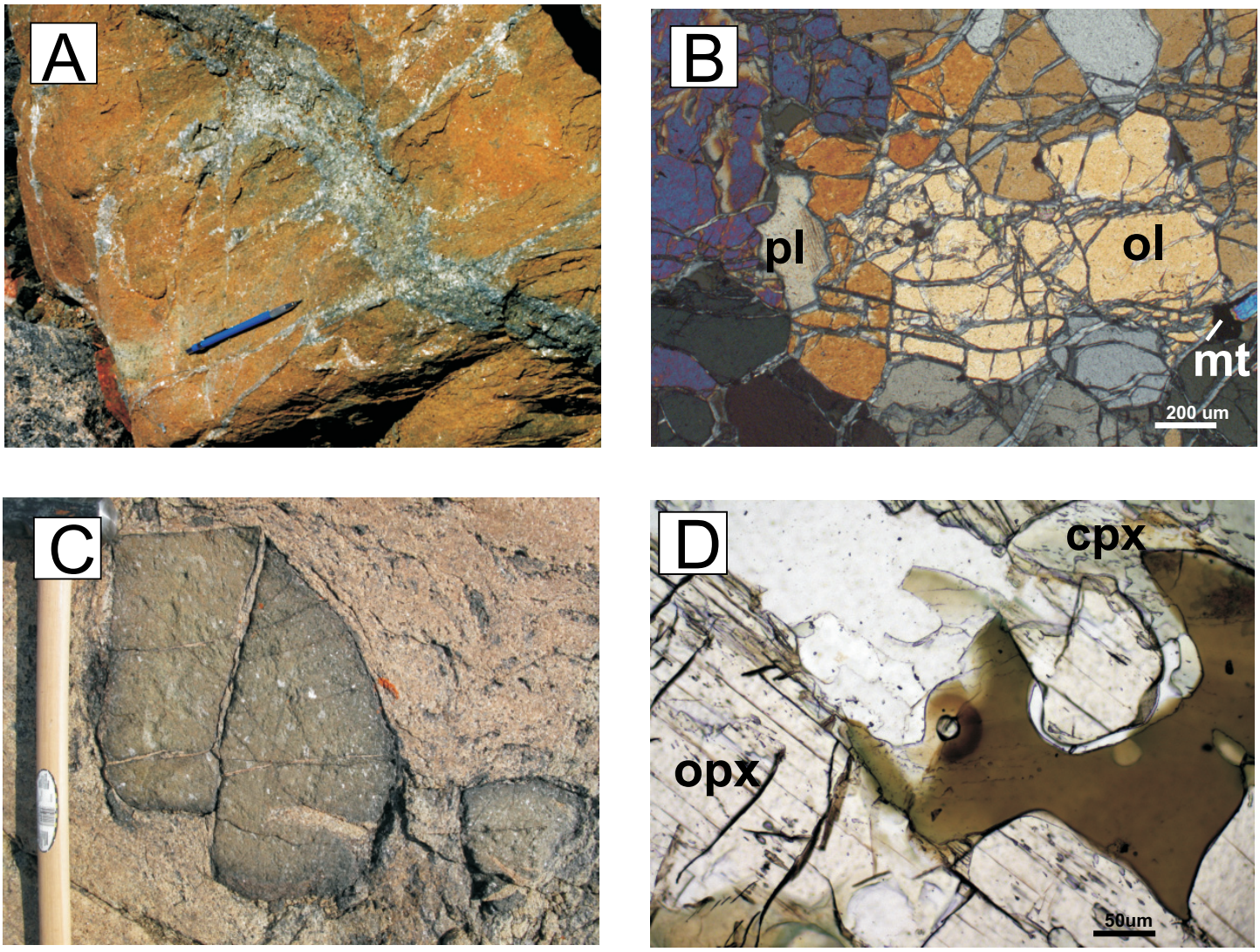

Figure 4. Representative pictures and photomicrographs of a dunite xenolith hosted TTG gneiss (A, B (crossed polars)) and a websterite xenolith hosted in enderbite (C, D (plane-polarized light)). Labels in Figure 4D are according to Whitney and Evans (2010).

defined by 5 to 10 cm thick compositional banding. Twenty percent of the unit takes the form of a stromatic metatexite migmatite, and locally as diatexite migmatite. This unit contains folded, dismembered, and boudinaged mafic dykes that are typically 1 to 2 m wide.

Within the eastern–central portion of the RBb, ca. 2.73–2.71 Ga biotite ± hornblende granodiorite and tonalite gneisses and migmatite, and sheets of clinopyroxene–hornblende metadiorite are exposed. In this region, hypersthene occurs as a prograde metamorphic mineral, replacing biotite. This unit is medium- to coarse-grained and yields a low (blue) signal in the combined aeromagnetic and total eU radiometric map (Fig. 3). Preserved xenocrystic zircon domains, Hf isotopic data, and zircon geochemistry reveal that ca. 2.86 Ga and ca. 2.73–2.71 Ga plutonism was derived from a ca. 3.25–3.10 Ga crust (LaFlamme et al. 2014a).

Charnockite and Granitoid Plutons

Hypersthene–augite–magnetite–biotite (± hornblende) enderbite with lesser charnockite (Unit 6) and biotite–hornblende ± augite granitoid (Unit 5) plutons intruded into, and commonly contain rafts of, the older TTG protoliths of the RBb. These plutons have been dated to be ca. 2.69–2.66 Ga (LaFlamme et al. 2014a). Charnockite plutons are massif-type and contain early igneous ortho- and clinopyroxene. Units 5 and 6 form large bodies throughout the southeastern portion of the RBb, forming a mottled high–low aeromagnetic signature, and a depleted (blue) eU radiometric signature (Fig. 3). These two units are homogeneous and massive in texture, becoming locally gneissic towards their outer margins. The foliation is defined by the alignment of biotite. Hafnium isotopic data and zircon trace element geochemistry reveal that this generation of magmatism was derived from both primitive and juvenile sources (LaFlamme et al. 2014a).

Ultramafic to mafic xenoliths typically occur within the plutons. Boudins of green dunite (Fig. 4A) composed of olivine + magnetite that is 10% altered to serpentine and phlogopite (Fig. 4B) are several metres in diameter. Based on their occurrence within lithologies preserving a depleted eU radiometric signal, these xenoliths are interpreted to outcrop within the plutons. The most common type of xenolith is websterite, which preferentially occurs in the enderbite portion of the pluton (Unit 6). Ultramafic websterite xenoliths (Fig. 4C) are up to 1 m in diameter, deep forest green in colour, medium grained,

Table 1. Analytical conditions for the geochemical analysis of olivine and pyroxene.

Mineral	Ablation mode	Crater Size (μm)	Ablation time (s)	Repetition Rate (Hz)	Fluence (J/cm^2)
Olivine	Linear Raster	48	30	10 (scan speed 5 μm/s)	5
Pyroxene	Drilling	124	40	5	10

and are composed of hypersthene–augite–plagioclase–magnetite with minor biotite and interstitial hornblende (Fig. 4D). Local exsolution of hypersthene occurred within the central portion of the augite grains. Monazite occurs as an accessory mineral. Mafic xenoliths are composed of hornblende with lesser amounts of biotite and clinopyroxene.

Metamorphism

The units of the RBb are polymetamorphosed, having undergone granulite-facies metamorphism twice since their formation (LaFlamme et al. 2014b). The earliest documented metamorphic event is localized and attributed to Neoarchean granulite-facies metamorphism associated with 2.69–2.66 Ga charnockitic plutonism in the lower to middle crust. This metamorphic event is discussed in further detail in this paper. Most recently, due to crustal thickening during the Paleoproterozoic Trans-Hudson orogeny, the units of the RBb underwent partial melting and ductile deformation at conditions of approximately 800°C and 9.5 kbar at ca. 1.82 Ga, followed by high temperature lateral extrusion (LaFlamme et al. 2014b).

METHODOLOGY

Whole Rock Chemical Compositions

Analyses were completed at Activation Laboratories Limited (Ancaster, Ontario, Canada) on rock powders prepared in a soft iron swingmill followed by lithium metaborate/tetraborate fusion and nitric acid dissolution of the fused bead then inductively coupled plasma–emission spectroscopy (ICP–ES) and ICP–mass spectrometry (MS). Major and trace elements were analysed by fusion ICP–ES in two separate batches. Each batch contained a method reagent blank, certified reference material and 17% replicates. Samples were mixed with a flux of lithium metaborate and lithium tetraborate and fused in an induction furnace. The melt was immediately poured into a solution of 5% nitric acid containing an internal standard, and mixed continuously until completely dissolved (~30 min). The samples were run for major oxides and selected trace elements (V, Cr, Co, Rb, Sr, Y, Zr, Nb, Cs, Ba, La, Ce, Pr, Nd, Sm, Eu, Gd, Tb, Dy, Ho, Er, Tm, Yb, Lu, Hf, Ta, Pb, Th, U, Be, Ni, Cu, Zn, Ga, Ge, As, Mo, Ag, In, Sn, Sb, W, Tl, Bi) on a Perkin Elmer Sciex ELAN 6000, 6100 or 9000 ICP–MS. Three blanks and five controls (three before sample group and two after) were analysed per group of samples. Duplicates were fused and analysed every 15 samples. The instrument was recalibrated every 40 samples. Calibration was performed using seven prepared USGS and CANMET certified reference materials. A total of four international standards were included as unknowns for quality control: NIM-D, NIM-N, MRG-1, SY-4.

Mineral Compositions

Major Elements

Major element analysis of mineral compositions for olivine and pyroxene was completed at the University of New Brunswick Microscopy and Microanalysis Facility by Energy Dispersive (X-ray) Spectrometry (EDS) using a JEOL6400 SEM equipped with an EDAX Genesis X-ray Microanalyser EDS operated at 1.5 nA and 15 kV with a focused beam. Spectra were collected for 60 s and spectrum background was removed by interpolation for each analysis. EDAX (Genesis) Energy Dispersive X-ray Analyser software was used to analyse and calibrate the energy spectrum in order to output the abundance of specific elements. RZAF (reverse ZAF) values (used to adjust beam current factor to account for the effect of atomic number, absorption within the sample detector and X-ray-induced fluorescence within the sample) were determined by comparing the measured and accepted values of a standard closely matching the unknown. Standards used for RZAF calibration were: 1, C.M. Taylor Company Multi-element standard mount No. 202-52 for diopside (AS1150-AB), and 2, Dunn SEM standard mount for olivine (1741) and orthopyroxene (alpine).

Trace Elements

Trace element geochemistry was completed by LA–ICP–MS at the University of New Brunswick, Department of Earth Sciences. Analyses were carried out using a Resonetics S-155 193 um ArF (excimer) laser ablation system coupled with a Agilent 7700x quadropole ICP–MS with two external rotary pumps and Iolite™ Trace Elements Data Reduction Scheme (Paton et al. 2011), running as a plug-in for Wavemetrics Igor Pro 6.22™. Quantitative measurements were collected for olivine (^{7}Li, ^{23}Na, ^{27}Al, ^{31}P, ^{43}Ca, ^{45}Sc, ^{47}Ti, ^{51}V, ^{52}Cr, ^{55}Mn, ^{59}Co, ^{60}Ni, ^{63}Cu, ^{66}Zn, ^{89}Y, ^{90}Zr, ^{93}Nb) and pyroxene (^{24}Mg, ^{29}Si, ^{43}Ca, ^{89}Y, ^{90}Zr, ^{93}Nb, ^{139}La, ^{140}Ce, ^{143}Nd, ^{147}Sm, ^{151}Eu, ^{155}Gd, ^{163}Dy, ^{166}Er, ^{173}Yb, ^{232}Th, ^{238}U). Dwell times for the individual analytes listed above were set between 0.01 and 0.05 s (approximately inversely proportional to the concentration in the target grain), for a total ICP–MS sweep time of about 0.5 s. To create ideal laser material coupling during ablation, conditions were varied for each mineral analysed in separate runs (Table 1).

The S-155 cell was pressurized with high purity He gas (at a rate of ~300 mL/min) and mixed in the cell with Ar (at a rate of 1000 mL/min). In each case, a background delay of 20 s was used. In the case of zircon, U–Pb ratios were analysed to ensure that trace elements were analysed from the magmatic domain of the grain. Concentration standard NIST-610 and one or two standards analysed as unknowns to ensure quality of data were included before and after each run using the same operating conditions. Standards analysed as unknowns included: GSE-1G, GORA-132G and GORA-128G. The ICP–MS was tuned using NIST-610 in order to maximize sensitivity while also monitoring oxide production (^{248}ThO$^+$/^{232}Th$^+$ < 0.3%), doubly charged ions (^{22}M$^+$/^{44}Ca^{++}< 0.4%), and plasma robustness (^{238}U$^+$/^{232}Th$^+$ = 1.05).

The total ICP–MS acquisition time was set to correspond to the total time to run through the predefined laser ablation sequence and the two instruments were operated simultaneously. To reduce the data Geostar laser log files and the Agilent time series data (cps versus time) were combined offline using the Iolite™ version 2.13 automatic integrations function, running as a plug-in for Wavemetrics Igor Pro 6.22™ (Paton et al. 2011). Independently measured (SEM–EDS) concentrations (elemental wt. %) of Mg in the minerals was used as an internal standard.

Elemental maps

Elemental (Fe, Mg, Ca, Mn) mapping of pyroxene was completed at the University of New Brunswick Microscopy and Microanalysis Facility on a JEOL733 electron probe microanalyser equipped with four wavelength dispersive spectrometers (WDS) and Geller dQuant automation software. The accelerating voltage was 15 kV and the amperage 100 nA.

RESULTS

The following section presents results from whole rock major and trace element (13 samples) and mineral (clinopyroxene, orthopyroxene, and olivine) chemical compositions. Appendix 1 lists the locations of samples analysed for whole rock and mineral chemical composition.

Whole Rock Major and Trace Element Compositions

The major and trace element composition of 13 samples from the RBb are described in this section and presented in Table 2. The results are presented in two divisions including ca. 2.69–2.66 Ga pyroxene and non-pyroxene bearing granitoid rocks (5 samples), and xenoliths hosted within the granitoid rocks (7 samples: 6 websterite, 1 gabbro). A single sample from a dunite xenolith is also presented.

Alteration and partial melting can obscure primary magmatic trends by redistributing mobile elements. Care was taken to choose samples that preserved an unaltered igneous texture. Figure 5 plots selected major and trace elements from the 13 samples against Zr and Mg# to identify differentiation trends. Zr is an element known to be incompatible in mafic melts and strongly partitioned into the residual melt during fractionation (Pearce and Norry 1979, also see Jenner 1996). The results yield a negative correlation between FeO and Zr and a positive correlation for SiO_2 and K_2O against Zr. Transitional elements (e.g. Co) behave in a relatively systematic manner. However, high field strength elements (HFSE; e.g. Ta) and REE (not shown) demonstrate scattered behaviour. Granitoid and xenolith lithologies show a pattern of increasing alkali (K_2O + Na_2O) and LILE (Ba + Sr) content, and a concave downwards pattern for the Al_2O_3 content with decreasing Mg#. Systematic trends suggest that these lithologies may be at least partially related by fractional crystallization processes. Two additional diagrams highlight the relationship between the granitoid and xenolith suites by crystal fractionation processes. The bivariate diagram Nb/Ta versus Zr/Hf plots two twin ratios of HFSE. Because each element in these ratios occurs in the same valence state, it is thought that both elements behave similarly during various geochemical processes. Figure 6A demonstrates a systematic trend between the two ratios, indicating a cogenetic relationship between both the granitoid and xenolith suites. Figure 6B (after Pearce and Norry 1979; Pearce 1982) is sensitive to crystal fractionation of olivine, clinopyroxene, and orthopyroxene (which causes a rise in Zr and Ti) versus magnetite, biotite, and amphibole (which causes a decrease in Zr and Ti). What is important to note is that both the granitoid and xenolith suites lie on a single trend line that indicates that they were likely formed by crystal fractionation processes.

Granitoid and xenolith lithologies plot in the subalkaline field (Fig. 7A) of the SiO_2 versus total alkalis diagram of Irvine and Baragar (1971) and dominantly in the magnesian field (Fig. 7B) of the $FeO_T/(FeO_T + MgO)$ versus SiO_2 field of Frost et al. (2001). The ca. 2.69–2.66 Ga granitoid lithologies are SiO_2-rich (63.6–71.4 wt. %), with high $Na_2O + K_2O$ contents (up to 8.5 wt.%) and have a Mg# = 13–24 (Mg# = 100 * molecular $MgO/(MgO + FeO_T)$). Websterite and gabbro xenoliths hosted in the 2.69–2.66 Ga granitoid lithologies are SiO_2-poor (49.7–54.5 wt. %), and have a Mg# = 41–66. Transition element contents are low in granitoid lithologies (Cr < 30 ppm; V < 76 ppm; Ni < 10 ppm) and high in mafic to ultramafic xenoliths (Cr: 370–1080 ppm; V: 32–236 ppm; Ni: 90–1090 ppm). LILE contents in granitoid lithologies are high (Ba + Sr = up to 2239 ppm). One sample from a dunite xenolith (composed of olivine (90%) + spinel (2%) + phlogopite (8%)) contains 40% SiO_2 and a Mg# of 81. Transition elements within the dunite xenolith are high (Cr: 2440 ppm, Ni: 2800 ppm).

The chondrite-normalized REE profiles (normalizing values after Sun and McDonough 1989; Fig. 8A) for granitoid rocks and xenolith lithologies are nearly parallel. REE patterns in granitoid lithologies are moderately to highly fractionated (La_N/Yb_N = 4–54), whereas, REE patterns in xenoliths are moderately fractionated (La_N/Yb_N = 1–3). The granitoid lithologies exhibit a slightly negative to slightly positive Eu anomaly (Eu_N/Eu_N^* = 1.1); whereas the xenoliths yield a moderately negative Eu anomaly (Eu_N/Eu_N^* = 0.6). The dunite xenolith is also moderately fractionated (La_N/Yb_N = 0.9), with moderate LREE contents (La_N = 1.3) and low HREE contents (Yb_N = 1.4).

An extended chondrite-normalized trace element plot (normalizing values after Sun and McDonough 1989; Fig. 8B) demonstrates that for all samples the elements Nb, Ta, and Ti are depleted relative to LILE. The same plot demonstrates that the elements Zr and Hf are enriched with respect to the medium rare earth elements (MREE) within the granitoid units and depleted in the websterite and gabbro xenoliths.

Mineral Compositions

The mineral chemical composition of orthopyroxene and clinopyroxene from a sample of an enderbite intrusion (10CXAL190A01) and a websterite xenolith (10CXAL134B01), as well olivine from a sample of a dunite xenolith (10CXAL249A01) were analysed for major elements by EDS and trace elements by LA–ICP–MS. Major and trace element geochemical compositions are presented in Table 3. Raw analytical data for pyroxene and olivine trace element compositions are presented in Appendices 2 and 3, respectively.

Clinopyroxene and orthopyroxene fall within a solid solution between diopside ($CaMgSi_2O_6$), hedenbergite ($CaFeSi_2O_6$), enstatite ($Mg_2Si_2O_6$), and ferrosilite ($Fe_2Si_2O_6$). In this case, clinopyroxene in the enderbite intrusions yields a composition

Table 2. Whole rock major and trace element geochemical compositions.

Sample[a]	L249A-01	L001B-03	L194B-01	L134B-01	L131B-01	L001B-02	L001B-01	L001C-01	L190A-01	D003A-01	L118A-01	N031A-01	L184A-01
Lithology[b]	dunite	web	web	web	web	web	web	gabbro	end	ch	gd	g	gd
Location	1	2	3	4	5	2	2	2	6	1	7	8	9
Easting[c]	545100	643251	652390	639402	638853	643251	643251	643251	652515	643251	631908	697030	681910
Northing[c]	7370000	7383655	7388158	7390775	7394339	7383655	7383655	7383655	7385280	7383655	7413757	7394330	7393372
Setting	xenolith	xenolith	xenolith	xenolith	xenolith	xenolith	xenolith	xenolith	main	main	main	main	main
Min. Ass.[d]	olivine	OCB	OCB	OCB	OCB	OCB	OCB	CB	OCBH	OCBH	BH	B	B
SiO_2	40.02	49.66	50.79	54.53	50.59	52.79	52.13	50.7	63.57	68.25	71.38	68.92	64.51
TiO_2	0.011	0.351	0.241	0.151	0.242	0.175	0.203	0.892	0.758	0.574	0.24	0.18	0.305
Al_2O_3	0.34	9.61	4.12	2.81	3.70	3.29	3.56	13.8	15.41	15.16	14.61	13.61	17.76
$Fe_2O_3(T)$	10.3	9.67	15.09	10.51	12.02	12.48	13.22	10.86	6.16	3.83	3.03	3.77	2.91
MnO	0.17	0.23	0.24	0.23	0.26	0.52	0.49	0.144	0.07	0.03	0.02	0.02	0.04
MgO	44.55	12.24	25.10	20.78	14.53	17.00	16.80	7.83	1.30	1.13	0.67	0.58	0.90
CaO	0.14	13.02	2.35	8.58	15.94	12.12	10.04	9.55	3.78	3.95	2.53	1.75	3.15
Na_2O	0.05	1.98	0.4	0.64	0.78	0.75	0.78	3.3	3.92	4.31	4.41	2.63	4.33
K_2O	0.15	0.69	0.39	0.41	0.3	0.54	0.68	1.19	2.79	1.16	2.09	5.46	4.15
P_2O_5	-	0.03	0.02	0.02	0.02	0.02	-	0.23	0.14	0.13	0.06	0.09	0.12
LOI	2.55	3.32	0.04	1.58	1.17	0.60	0.49	1.30	0.92	0.83	1.07	1.14	0.77
Total	98.29	100.80	98.78	100.24	99.56	100.30	98.39	99.80	98.81	99.34	100.10	98.15	98.96
Sc	4	55	20	21	12	12	15	34	13	4	2	1	3
Be	-	1	-	-	1	-	-	1	1	1	1	-	4
V	14	185	108	62	104	32	46	236	76	69	21	38	31
Cr	2440	650	1080	1580	1020	1000	740	370	-	30	-	-	-
Co	114	37	109	58	66	47	35	37	11	6	4	5	5
Ni	2800	190	870	1050	1090	910	650	90	-	-	-	-	-
Cu	-	-	40	-	190	-	-	50	40	30	40	80	10
Zn	160	110	120	140	240	250	200	80	610	500	420	680	40
Ga	1	10	7	8	11	11	8	18	22	19	19	17	24
Ge	1.2	2.5	1.7	2.3	2.9	3.3	2.5	1.8	1.4	0.8	0.9	1.1	1.5
As	-	-	-	-	-	-	-	-	10	-	6	15	-
Rb	10	6	15	19	7	19	19	14	44	10	48	153	136
Sr	5	102	72	34	45	40	47	359	242	434	332	327	392
Y	0.5	18	4.5	28.9	9.8	37.4	24.8	20.7	18.4	3.7	2.3	4	6.3
Zr	4	15	25	21	24	31	18	95	212	135	140	237	208
Nb	-	3.2	1.1	1.3	2.0	3.6	2.8	4.6	12.6	4.3	3.2	1.8	7.4
Mo	-	-	-	-	-	-	-	-	-	-	-	-	4
Ag	-	-	-	-	-	-	0.7	-	-	-	-	-	-
In	-	-	-	-	-	-	-	-	0.1	-	-	0.1	-
Sn	-	2	-	8	2	2	1	-	3	1	-	1	1
Sb	1.2	0.2	0.6	0.3	0.9	2.3	2	-	0.5	-	-	1	-
Cs	0.2	-	0.1	0.2	-	0.1	-	-	-	-	-	-	1.5
Ba	13	73	181	61	106	189	191	353	1051	435	460	1912	982
La	1.25	12.8	5.26	13.8	16.3	14.3	9.9	33.9	27.6	29.0	14.0	99.0	34.4
Ce	2.54	34.2	10.4	46.7	39.0	52.2	34.8	75.1	55.5	47.2	22.0	165	59.5
Pr	0.33	4.23	1.2	7.36	4.4	7.89	5.43	9.43	7.18	4.78	2.13	15.8	6.22
Nd	1.02	16.3	4.49	32.2	14.9	33.6	22.9	36.9	30.5	16.1	6.89	45.7	20.4
Sm	0.47	3.7	0.89	8.39	2.61	8.49	5.78	6.86	6.96	2.16	1.01	4.48	3.4
Eu	0.107	0.862	0.217	0.596	0.671	1.3	0.768	1.62	1.12	0.819	0.595	0.708	0.899
Gd	0.21	3.39	0.92	6.77	2.17	7.41	5.10	5.62	6.12	1.44	0.65	1.85	2.23
Tb	0.04	0.58	0.14	1.08	0.32	1.26	0.83	0.81	0.9	0.16	0.09	0.18	0.28
Dy	0.2	3.37	0.85	6.04	1.88	7.35	4.70	4.11	4.57	0.74	0.42	0.76	1.2
Ho	0.04	0.66	0.17	1.12	0.36	1.41	0.94	0.82	0.79	0.13	0.08	0.13	0.21

(Continued)

Table 2. Whole rock major and trace element geochemical compositions. *(Continued)*

Sample[a]	L249A-01	L001B-03	L194B-01	L134B-01	L131B-01	L001B-02	L001B-01	L001C-01	L190A-01	D003A-01	L118A-01	N031A-01	L184A-01
Lithology[b]	dunite	web	web	web	web	web	web	gabbro	end	ch	gd	g	gd
Location	1	2	3	4	5	2	2	2	6	1	7	8	9
Easting[c]	545100	643251	652390	639402	638853	643251	643251	643251	652515	643251	631908	697030	681910
Northing[c]	7370000	7383655	7388158	7390775	7394339	7383655	7383655	7383655	7385280	7383655	7413757	7394330	7393372
Setting	xenolith	xenolith	xenolith	xenolith	xenolith	xenolith	xenolith	xenolith	main	main	main	main	main
Min. Ass.[d]	olivine	OCB	OCB	OCB	OCB	OCB	OCB	CB	OCBH	OCBH	BH	B	B
Er	0.18	1.85	0.49	2.99	1.06	4.04	2.62	2.32	1.93	0.37	0.21	0.37	0.55
Tm	0.037	0.262	0.072	0.41	0.155	0.582	0.384	0.349	0.236	0.046	0.029	0.051	0.084
Yb	0.24	1.7	0.52	2.45	0.99	3.62	2.50	2.21	1.31	0.28	0.19	0.31	0.55
Lu	0.036	0.26	0.099	0.371	0.152	0.539	0.402	0.333	0.192	0.041	0.031	0.047	0.088
Hf	0.1	0.5	0.6	0.9	0.6	1.1	0.5	2.5	4.7	2.9	3.2	5.6	4.9
Ta	0.03	0.17	0.12	0.12	0.23	0.43	0.16	0.14	0.33	0.18	0.08	-	0.27
W	-	-	-	-	-	-	-	1.1	1.8	-	-	-	10.8
Tl	-	-	0.09	0.09	0.10	0.08	-	0.09	0.65	0.14	0.36	1.10	0.79
Pb	-	-	-	-	-	-	-	9	149	151	144	275	32
Bi	-	-	-	-	0.2	-	-	-	0.3	0.2	0.3	0.9	0.2
Th	0.53	0.87	1.8	3.67	0.52	3.02	0.97	2.5	0.43	1.1	1.04	42	5.4
U	0.09	0.11	0.22	0.21	0.05	0.29	0.16	0.26	0.46	0.25	0.22	0.98	2.44

[a] Concentration of oxides are reported in wt. % and trace elements in ppm.
[b] Lithology abbreviations: web – websterite, end – enderbite, ch – charnockite, gd – granodiorite, g – granite.
[c] UTM coordinates in NAD83.
[d] Mineral associations (Min. Ass.) denote the mafic mineral components of the unit: O – orthopyroxene, C – clinopyroxene, B – biotite, H – hornblende.
For sample locations, see Figure 2.

of XWo: 45.9, XEn: 36.7, and XFs: 17.4, whereas, in the websterite xenolith yields a composition of XWo: 47.3, XEn: 44.3 and XFe: 8.4. Orthopyroxene in the enderbite intrusion yields a composition of XWo: 1.2, XEn: 49.2, and XFs: 49.6, whereas, in the websterite xenolith yields a composition of XWo: 0.9, XEn: 75.7 and XFe: 23.5. Clinopyroxene preserves a high Mg# in the enderbite intrusion (Mg# = 66) and in the websterite xenolith (Mg# = 85).

In chondrite-normalized REE plots (normalizing values after Sun and McDonough 1989; Fig. 9A), orthopyroxene in both samples contains sub-parallel REE patterns that are enriched in HREE compared to LREE (La_N/Yb_N=0.03–0.60) when normalized to chondrite values (Sun and McDonough 1989), with a distinct negative Eu anomaly (Eu_N/Eu_N^* = 0.13–0.37). Clinopyroxene in both samples preserves a nearly flat REE profile (La_N/Yb_N=1.4–3.3), with a distinct negative Eu anomaly (Eu_N/Eu_N^* = 0.17–0.28). However, in the websterite xenolith the REE profile is slightly convex upwards, whereas in the enderbite intrusion, the pyroxene REE profile is slightly concave upwards. Furthermore, clinopyroxene in the websterite xenolith contains a much higher REE content than in the enderbite intrusion. In primitive mantle-normalized trace element diagrams (normalizing values after Sun and McDonough 1989; Fig. 9B) all pyroxene grains have a negative anomaly in Zr compared to MREE. Pyroxene in the enderbite sample is depleted in both Th and Nb, while in the websterite sample is only depleted in Nb. Two-pyroxene thermometry (after Brey and Köhler 1990) yields a crystallization *T* of about 800 ± 15°C for the enderbite pluton and 749 ± 15°C for the websterite xenolith (assuming 20 kbar/75 km depth). These results reflect the temperature at which Ca–Fe–Mg diffusion ceased (Frost and Frost 2008).

Olivine ($[Mg,Fe]_2SiO_4$) mineral geochemistry was completed on a sample of dunite xenolith (10CXAL249A). The olivine in this sample occurs as Fo_{90} and yields high concentrations of Ni (3800 ppm), Zn (158 ppm), and Co (164 ppm) and low concentrations of Cr (6 ppm).

DISCUSSION

Relationship Between Granitoid Plutons and Entrained Ultramafic Xenoliths

Systematic behaviour for many major, compatible trace, and LIL elements versus Zr, suggests that these elements behave isochemically. Even the mobile elements (those with either low or high ionic potential) were not redistributed during metamorphism (Kerrich and Wyman 1996). Although the dataset is compositionally limited, we infer from Figure 5 a transitional trend in these elements that indicates that the granitoid and xenolith lithologies are related, and are considered to be at least in part the product of crystal fractionation. The observed scattered behaviour in HFSE and REE, plotted in Figure 5, is generally consistent with having arisen through fractional crystallization of a melt undergoing simultaneous assimilation (e.g. Rudnick et al. 1986). Figure 6 further strengthens this claim by demonstrating the cogenetic relationship between the granitoid and xenolith suites.

Whole rock analyses reveal a subalkaline, magnesian suite of ca. 2.69–2.66 Ga granitoid lithologies. The entrained dunite, websterite, and gabbro xenoliths within charnockite and granitoid lithologies yield subparallel chondrite-normalized REE

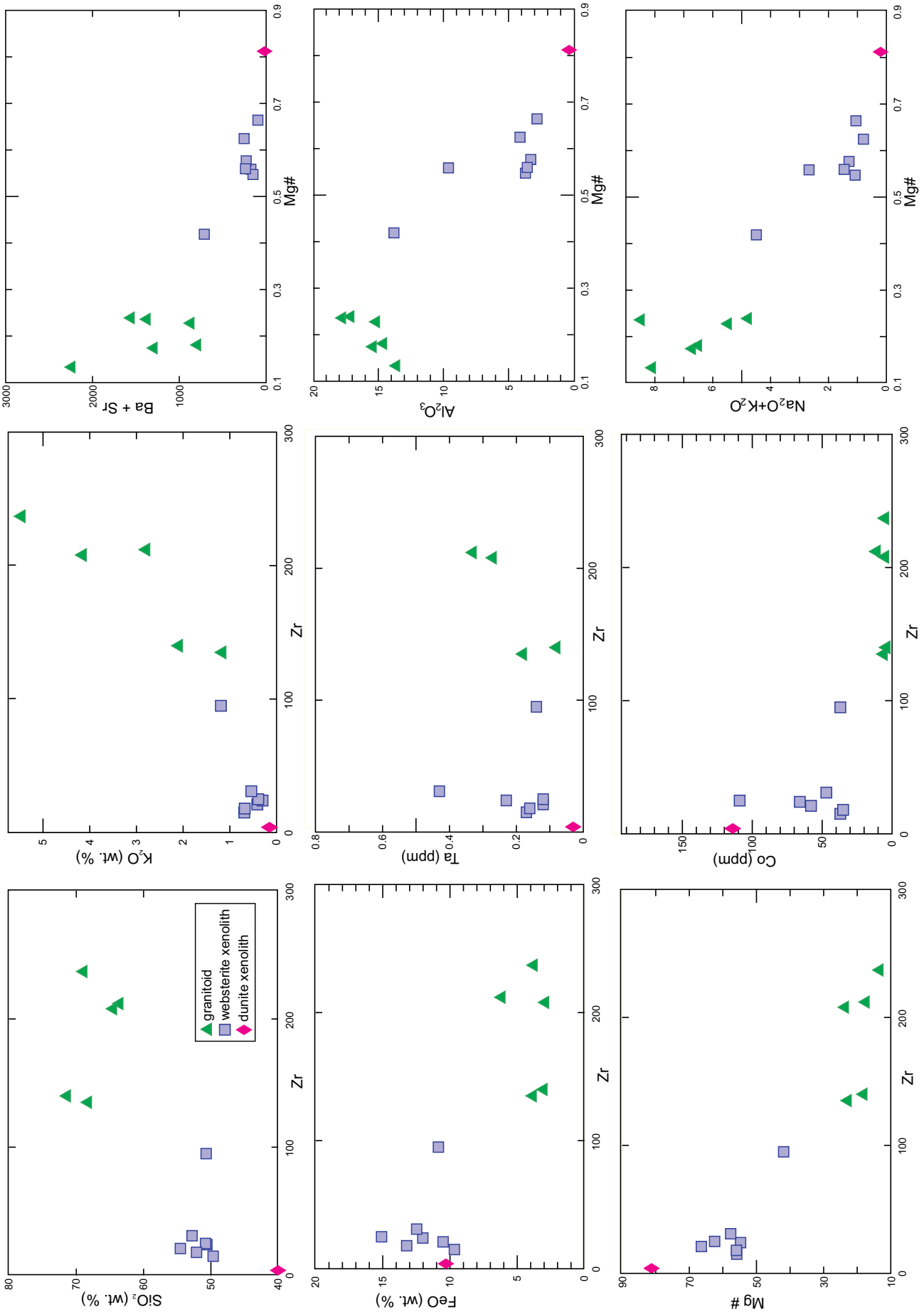

Figure 5. Selected major and trace element variation diagrams using Zr (ppm) and Mg# as a differentiation index.

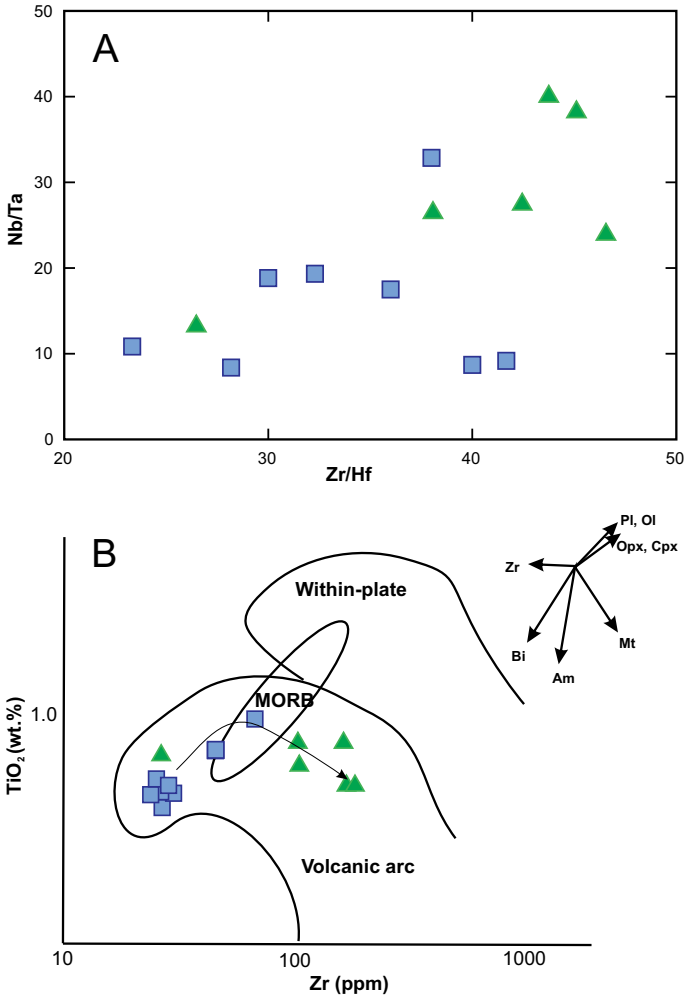

Figure 6. A) Bivariate diagram plotting Nb/Ta against Zr/Hf for the granitoid (triangles) and xenolith (squares) suites. B) Covariation diagram of TiO_2 versus Zr after Pearce and Norry (1979) to demonstrate that granitoid and xenolith suites lie on one trend line. Vector lines for olivine (Ol), plagioclase (pl), orthopyroxene (Opx), clinopyroxene (Cpx), magnetite (Mt), biotite (Bt), zircon (Zr), and amphibole (Am) after Pearce (1982).

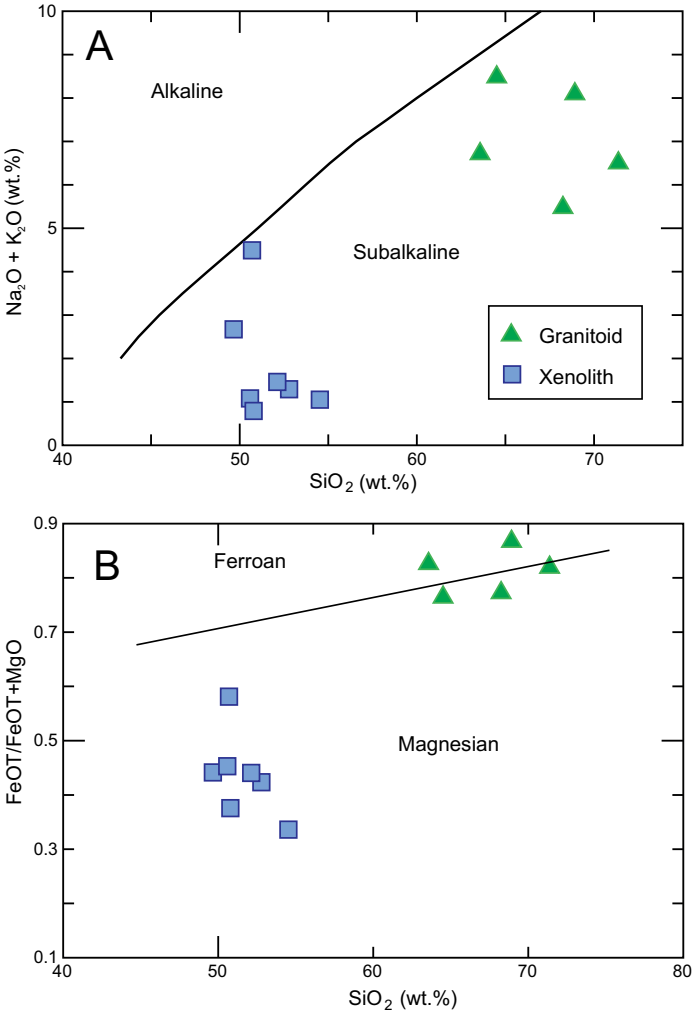

Figure 7. Repulse Bay block samples plotted on diagrams A) Na_2O+K_2O vs. SiO_2 (Irvine and Baragar 1971) and B) $FeO_T/(FeO_T + MgO)$ vs. SiO_2 (Frost et al. 2001).

patterns (Fig. 8A). These granitoid lithologies and xenoliths are moderately fractionated and exhibit LILE- and LREE-enriched, primitive mantle-normalized incompatible rare element patterns with moderate to significant Ta, Th, and Ti troughs (Fig. 8B). The Eu anomaly ranges from slightly negative to slightly positive indicating a progressive depletion in Eu^{2+} during plagioclase crystallization. The only distinct difference between xenoliths and granitoid lithologies is the concentration of primitive mantle-normalized Sr, Hf, and Zr ratios that are depleted compared to primitive mantle-normalized MREE ratios in websterite xenoliths (discussed below).

Pyroxene mineral compositions from an enderbite intrusion and websterite xenolith yield systematically parallel pyroxene trace element plots with only slight differences in primitive mantle-normalized Th and Nb concentrations, and in REE patterns in clinopyroxene. The clinopyroxene in the websterite xenolith has a convex-upward chondrite-normalized REE pattern. Both features are consistent with having formed as deep level cumulate crystals (Irving and Frey 1984; Deer et al. 1992).

When normalized against the primitive mantle, a dunite (olivine + phlogopite + magnetite) xenolith, occurring within the Neoarchean granitoid gneiss, displays a mantle-like signature including high Ni contents (2440 ppm) and high Mg# (81) in whole rock, and high forsterite content (Fo_{90}) and Ni content (4000 ppm) in olivine. These features are consistent with derivation from mantle melts (Sato 1977; Sano et al. 2002; de Hoog et al. 2010). Low Cr contents in olivine (6 ppm) compared to other mantle-derived lherzolite examples (de Hoog et al. 2010) is interpreted to reflect sequestering of Cr in phlogopite over olivine. The dunite xenolith also contains a whole rock signature which may be consistent with crustal contamination including LILE and LREE enrichment, and negative Nb, Ti and Y anomalies. However, based on a relatively low forsterite content in olivine compared to olivine found in typical subcontinental mantle lithosphere lherzolite xenoliths (Mg# in olivine ~93; e.g. Schmidberger and Francis 1999; Griffin et al. 2003, 2009), the dunite xenolith is interpreted to represent a cumulate-type magma, derived during Archean magmatism.

Given the decrease in Mg# and progressive increase in LILE and alkali content, it is possible that these lithologies record fractionation of a primitive magma during its passage through the mantle and the crust. The concave-down nature of Mg# vs. Al_2O_3 content is a feature consistent with the progressive fractional crystallization of clinopyroxene (e.g. Ohba

Table 3. Major and trace element mineral geochemical composition.

Sample[a] (10CXAL)	190A01	190A01	134B01	134B01	249A01
Lithology	enderbite	enderbite	websterite	websterite	dunite
Setting	main	main	xenolith	xenolith	xenolith
Mineral[b]	clinopyroxene	orthopyroxene	clinopyroxene	orthopyroxene	olivine
SiO_2	51.5	51.74	53.1	55.47	40.81
TiO_2	0.10	0.07	0.15	0.08	
Al_2O_3	1.33	0.91	1.91	0.98	
$Fe_2O_{3(T)}$	10.59	29.83	5.16	14.9	8.93
MnO	0.33	0.79	0.10	0.33	
MgO	12.5	16.61	15.35	26.93	48.92
CaO	21.75	0.58	22.81	0.42	
Na_2O	0.5	0.22	0.92	0.19	
K_2O	0.07	0.03	0.00	0.08	
Total	98.74	100.78	100.11	99.52	98.67
Si	184500	261400	240220	268800	
Ca	18920	5034	153878	3484	404
Y	15.95	16.30	77.41	2.60	0.06
Zr	0.260	0.235	29.705	0.447	0.112
Nb	0.042	0.013	0.090	0.011	0.020
La	10.750	0.578	19.703	0.232	
Ce	14.400	1.132	94.120	0.660	
Nd	5.880	0.611	86.570	0.515	
Sm	1.106	0.305	23.013	0.166	
Eu	0.097	0.022	1.335	0.014	
Gd	1.351	0.688	20.330	0.203	
Dy	2.468	2.346	16.818	0.352	
Er	2.459	2.603	7.779	0.376	
Yb	3.407	4.017	6.177	0.719	
Th	0.001	0.001	0.336	0.018	
U	0.003	0.001	0.135	0.013	
Li					3.9
Na					379
Al					10
P					19
Sc					15
Ti					7.8
V					0.48
Cr					128
Mn					1608
Co					163
Ni					3824.8
Cu					0.08
Zn					164

[a] Oxides are reported in wt. %, trace elements and Si, Ca are reported in ppm
[b] Mineral analysed

et al. 2009). Therefore, field, petrographic, and geochemical evidence exists in the RBb for large-scale fractional crystallization (e.g. magmatic layering, similar mineral assemblages between xenoliths and host lithologies, and similar whole rock and pyroxene trace element patterns). To account for the enrichment of fluid mobile elements like LREE, neither notable in the metasomatized mantle nor in slab melts, fractional crystallization processes are interpreted to have undergone concurrent assimilation with the solid wall rocks surrounding a magma chamber. The process is known as assimilation-fractional crystallization (DePaolo 1981). Therefore, based on similar mineralogy (orthopyroxene–clinopyroxene–biotite–plagioclase), petrographic features, and similar whole rock and pyroxene geochemical properties, the xenoliths and host charnockite and granitoid intrusions are interpreted to preserve a cogenate relationship rather than representing discrete magmatic events. The cumulate websterite xenoliths (now known as autoliths) may represent early crystallized units approaching the parental composition.

Sanukitoid Affinity of Neoarchean Intrusions

The presence of negative Nb, Ta, and Ti anomalies and enrichment of the LILE relative to the HFSE are characteristic features of volcanic arc magmas (Pearce 1982); however, these trace element compositions are not exclusive to arc magmatism. The retention of ~2% rutile in a mafic source can also generate these anomalies (Bédard 2006; Bédard et al. 2013). This 'arc-like' geochemical signature is also typical in Archean TTG and sanukitoid lithologies worldwide (e.g. Martin et al. 2005 and references therein). The sanukitoid suite is composed of Neoarchean granitoid lithologies that contain both an 'arc-like' and 'mantle-like' chemical signature that reflects their generation from a mantle peridotite source, rich in incompatible elements (Laurent et al. 2014 and references therein). Geochemically, the sanukitoid suite can vary depending on the physical conditions in which it was generated; however, the suite is always calc-alkaline, metaluminous, and commonly contains Mg# > 0.6, Ni > 100 ppm, Cr > 200 ppm, K_2O > 1%, Ba + Sr > 1000 ppm, enrichment in LREE, and little to no Eu anomaly (Stern et al. 1989).

In the RBb, websterite autoliths preserve a high Mg# (up to 0.66) and high Cr (650–1580 ppm) and Ni (90–1090 ppm) contents. Although the more differentiated granitoid lithologies do not preserve an obvious geochemical mantle signature, they do contain high alkali, Ba, and Sr contents, geochemical signatures that are interpreted to be indicative of mantle input (e.g. Walter 2003). The ca. 2.69–2.66 Ga granitoid rocks and autoliths are enriched in LREE and have a variable positive to negative Eu anomaly (Fig. 8). These features are consistent with the known geochemical properties of sanukitoid magmatism during ongoing fractional crystallization (e.g. Smithies and Champion 2000; Martin et al. 2005; Halla 2005; Heilimo et al. 2010; 2013; Laurent et al. 2013). Furthermore, the enderbite and websterite xenolith lithologies preserve an elevated Mg# in clinopyroxene (websterite xenolith = 85, enderbite intrusions = 66), similar to the Mg# in clinopyroxene in the Roaring River sanukitoid intrusion in the Superior Province (Stern and Hanson 1991) and the Panozero intrusion in the Karelian craton of the Baltic Shield (Mg# = 72–75; Lobach-Zhuchenko et al. 2008).

Melt Derivation

The Hf isotopic signature from ca. 2.69–2.66 Ga sanukitoid-type granitoid rocks in the RBb yields a wider range of initial εHf values (–7.1 to +1.0) than earlier ca. 2.73–2.71 Ga TTG-type magmatism (–4.8 to –2.4). This isotopic signature is a reflection of derivation of an isotopically juvenile source that interacted with an evolved crustal source. Based on the large

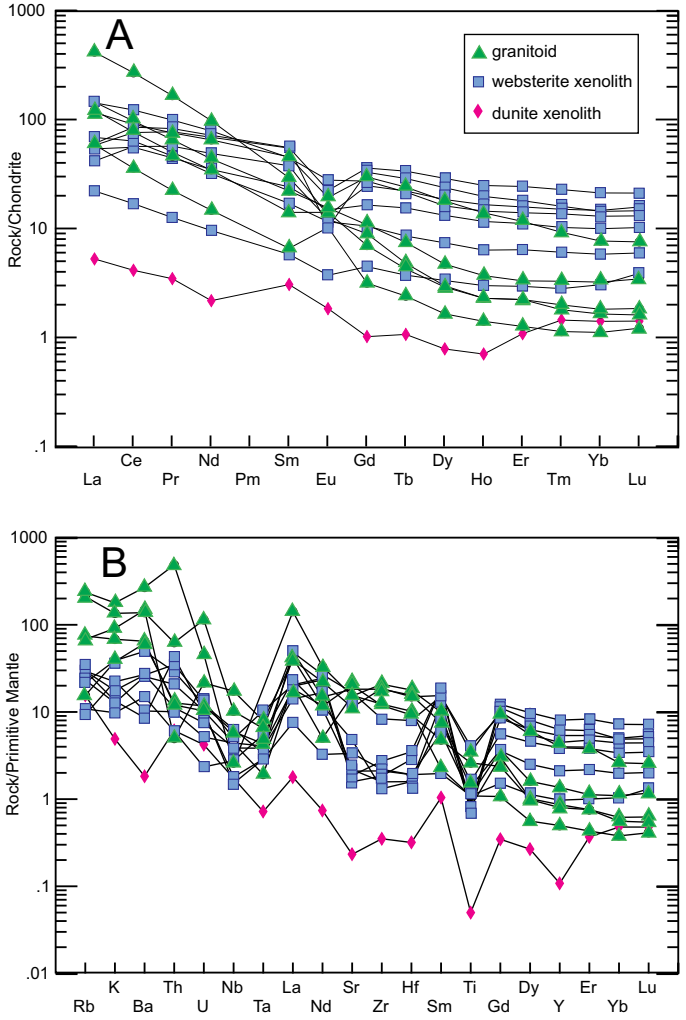

Figure 8. A) Chondrite-normalized REE plot (normalized values taken from Sun and McDonough 1989) for granitoid intrusions and xenoliths. B) Primitive mantle-normalized extended trace element diagram (primitive mantle-normalizing values taken from Sun and McDonough 1989).

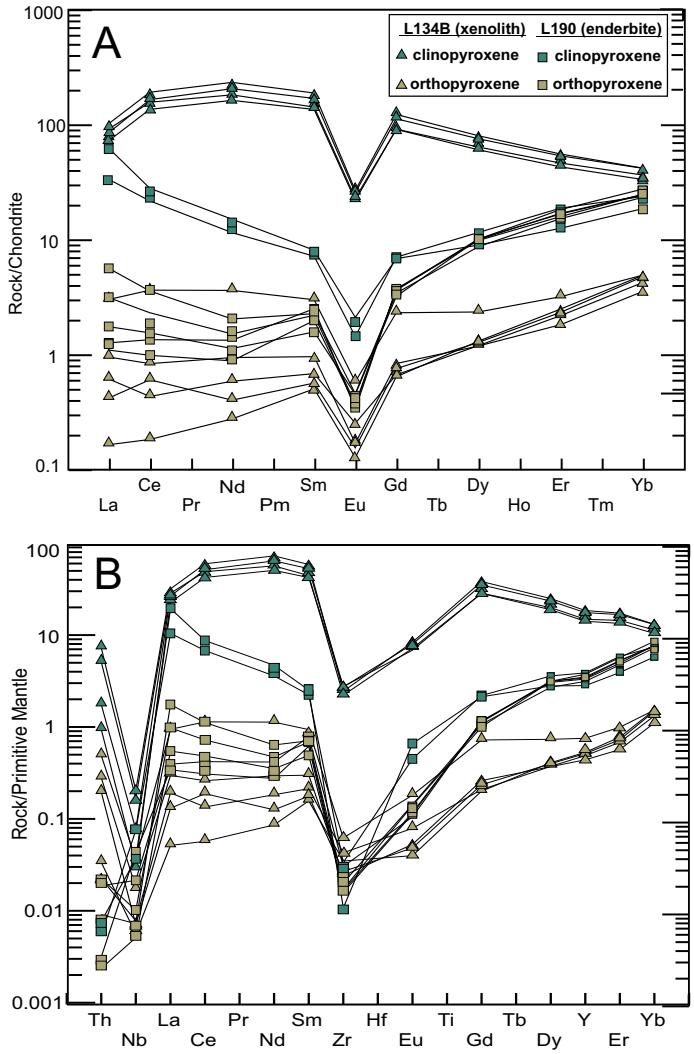

Figure 9. A) Chondrite-normalized REE plot (normalizing values taken from Sun and McDonough 1989) for orthopyroxene and clinopyroxene in enderbite intrusion and websterite xenolith. B) Primitive mantle-normalized extended trace element diagram (primitive mantle-normalizing values taken from Sun and McDonough 1989).

volume of exposed anhydrous magmatism and the geochemical signature of the cumulate-type websterite and dunite xenoliths, the juvenile source is interpreted to be derived directly from the primitive mantle.

Recycling of crust into the mantle occurs during accretion of island arcs at convergent margins. This type of accretion is proposed to have been the primary mechanism during amalgamation of the Slave and Superior cratons in the Archean (e.g. Ketchum et al. 2004; Davis et al. 2005). Based on a geochemical modelling of Sr, Nd, Hf, $\delta^{18}O$ values and trace elements, a number of authors have demonstrated that within a subduction zone setting, crustal reservoirs were the source of mantle enrichment to form the sanukitoid rocks in the Karelia, Baltic, Amazonia, Dharwar cratons, etc. (Fig. 10; Moyen et al. 2001; Lobach-Zhuchenko et al. 2005; de Oliveira et al. 2011; Heilimo et al. 2013). These sanukitoid intrusions are isotopically similar to comparable rocks in the Superior and Slave cratons of the Canadian Shield (Heilimo et al. 2013, and references therein), demonstrating that the same crustal formation processes were occurring within the Rae craton as well.

Because Zr and Hf are hosted by zircon in subduction zones (Rubatto and Hermann 2003), a residue containing accessory zircon, is likely controlling the Zr and Hf levels in websterite xenoliths. Metasomatism of the mantle by hydrous slab melts may have led to the enrichment of Zr and Hf (Rubatto and Hermann 2003) in the later cumulate products. In addition, the most evolved granitoid rocks contain the highest ferroan content, which are known to be derived from oxidizing slab melts that carry ferric iron in solution (Mungall 2002). Finally, the clinopyroxene chemical compositions demonstrate that REE were most abundant during the earlier stages of crystallization, which may indicate that the mantle was enriched in REE. These three features suggest that metasomatism of the primitive mantle by slab melts is an important component in Neoarchean magma generation.

The development of a metasomatically enriched lithosphere occurs by melting and hybridization of the mantle wedge with slab-derived crustal melts during subduction toward the end of the Archean (Moyen et al. 2001). An enriched (metasomatized) mantle is a prominent feature of the Neoarchean due to the effects of steeper subduction than in the earlier Archean. The breakdown of hydrous phases in sub-

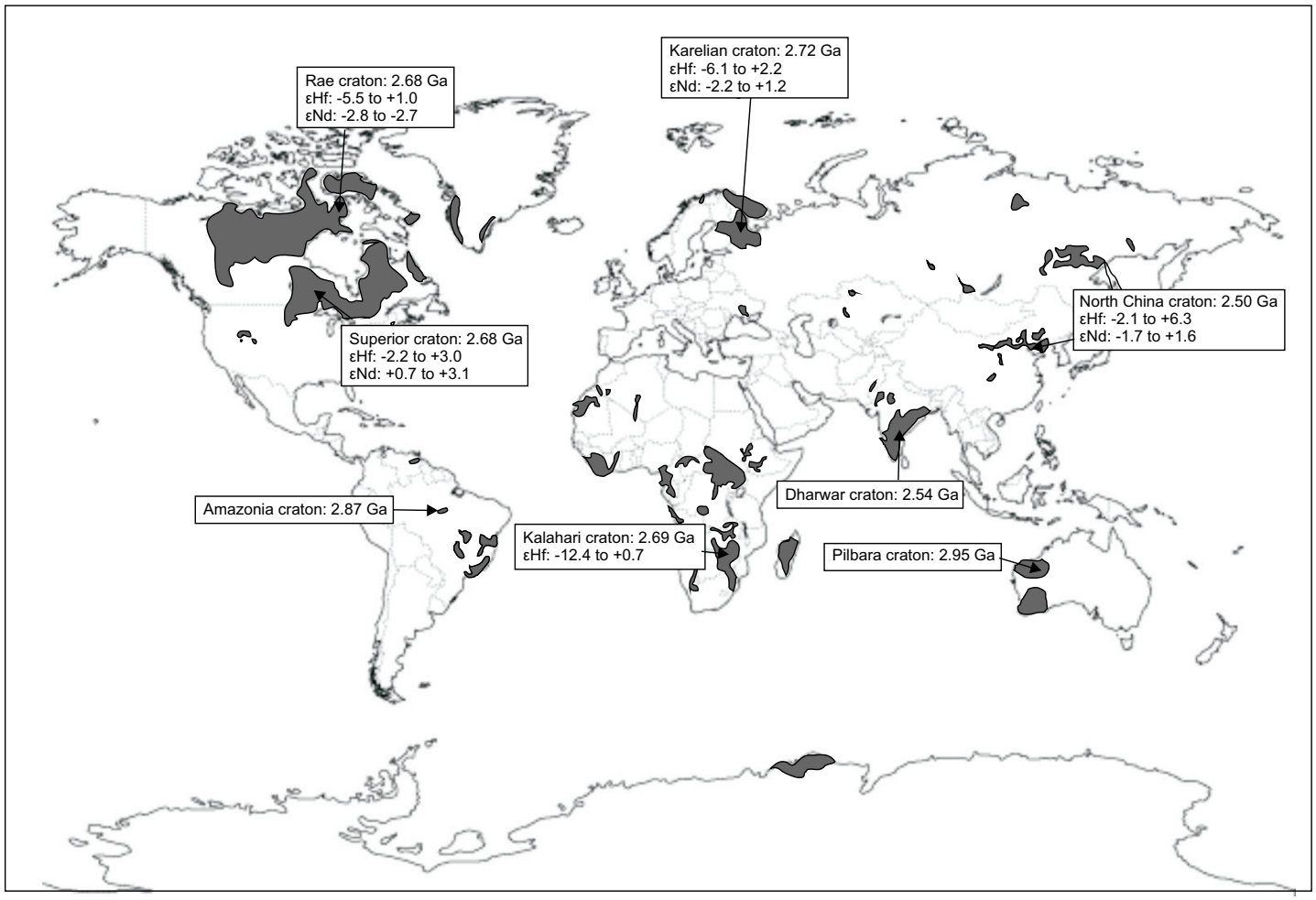

Figure 10. Location of some recognized sanukitoid magmatism worldwide. Global distribution of exposed Archean crust is in gray (modified after Bleeker 2003). Sanukitoid magmatism is found in the Karelian craton (Heilimo et al. 2013 and references therein), the Pilbara craton (Smithies and Champion 2000), the Superior craton (Stern and Hanson 1991; Davis et al. 2005), the Dharwar craton (Moyen et al. 2001 and references therein), the Kalahari craton (Zeh et al. 2009), the Amazonia craton (de Oliveira et al. 2009), the North China craton (Ma et al. 2013), and the Rae craton (this study).

ducting crust results in the formation of phlogopite and richterite in the upper mantle (Schmidt and Poli 1998). Thus, LILE enrichment within the mantle occurs by way of the sequestering of LILE in phlogopite, known to occur within a subduction zone setting at depth (Wyllie and Sekine 1982). Significant water and alkali contents existing in the mantle derived from slab melts may be the reason for the development of hydrous phases (interstitial biotite and amphibole) within the ultramafic autoliths and charnockitic intrusions (e.g. Ionov et al. 2002). For example, geochemical and isotopic evidence indicates a metasomatically modified mantle source in the nearby Hearne craton (Sandeman et al. 2003).

A number of mechanisms for sanukitoid melt derivation have been proposed in recent years to account for both mantle-derived and crust-contaminated geochemical and isotopic signatures. They include: 1) partial melting of a metasomatized mantle and assimilation of TTG crust (Smithies and Champion 2000; Moyen et al. 2001; de Oliveira et al. 2011); 2) partial melting of a metasomatized mantle hybridized by Archean sedimentary rocks (Heilimo et al. 2013) or fluids derived from Archean sedimentary rocks (Halla 2005); 3) an interplay among multiple processes including fractional crystallization, assimilation-fractional crystallization, and binary magma mixing (Laurent et al. 2013); 4) hybridization of TTG melts by assimilation of an olivine-bearing peridotite (Rapp et al. 2010); and 5) crystal fractionation through anatexis of lower crustal rocks (Qian and Hermann 2010). Laurent et al. (2014) pointed out that the global granitoid diversity associated with the sanukitoid suite reflects different petrogenetic processes occurring at mantle depths and, in particular, the specific nature and composition of the metasomatic agent. We propose here that the sanukitoid suite of the RBb was derived from a metasomatically enriched sub-continental lithospheric mantle that interacted with the base of the not yet refractory continental crust.

Conditions of Emplacement

The two-pyroxene thermometer of Brey and Köhler (1990) preserves Ca–Mg–Fe exchange temperatures that are much too low to reflect the crystallization temperature of the websterite xenoliths and enderbite intrusions. Based on the results from two-pyroxene thermometry and the homogeneous Fe and Mg content of pyroxenes preserved in the websterite xenolith (Fig. 11A) and enderbite intrusion (Fig. 11B), pyroxene thermometry is interpreted to have been reset by granulite-facies metamorphism during the Paleoproterozoic Trans-Hudson orogeny and exchange of Ca–Mg–Fe. It should also be

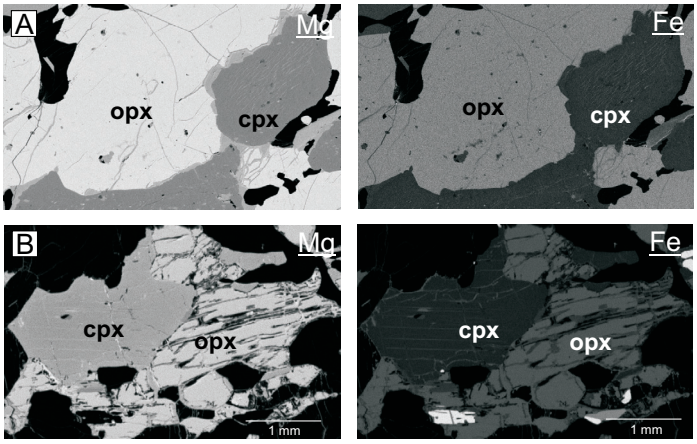

Figure 11. Magnesium and iron elemental maps by EMP analysis of pyroxenes in a websterite xenolith (A; 10CXAL134B) and enderbite intrusion (B; 10CXAL190A).

noted that erroneous *T* measurements for two-pyroxene thermometry have previously been reported for granulites devoid of spinel and olivine (e.g. Roach 2004).

TTG magmas form in different tectonic settings at melting pressures ranging from < 10 kbar to > 25 kbar, affecting residue mineralogy and trace element composition (Moyen and Stevens 2006; Moyen 2011; Nagel et al. 2012; Qian and Hermann 2013). Although sanukitoid magmas are known to be sourced from mantle that was metasomatized by melts, the nature of the sanukitoid series is strongly dependent on the pressure of magma generation (de Oliveira et al. 2011; Laurent et al. 2014). The sanukitoid suite from the RBb is relatively depleted in HREE compared to LREE contents in whole rock (see Fig. 8) indicative of garnet retention in the residue (Drummond and Defant 1990). This is in accord with the trace element zircon data presented by LaFlamme et al. (2014a) that demonstrates that both the ca. 2.73–2.71 Ga TTG gneiss and ca. 2.69–2.66 Ga granitoid rocks in the RBb formed from a source containing garnet.

Figure 12 demonstrates two typical Archean geotherms for a down-going oceanic plate in a subduction zone (after Foley 2008). The down-going amphibolite oceanic slab likely melted between the two geotherms in the 'garnet-present' field at *P*–*T* conditions of > 800°C and > 8 kbar to contribute (along with crustal reworking) to the intrusion of a ca. 2.73–2.71 Ga granitoid (granite, granodiorite, tonalite, trondhjemite) crust. These conditions are consistent with the findings of Moyen and Stevens (2006). The slab (now of a garnet–amphibole–pyroxenite composition) then melted again at $T > 1000$°C and $P >$ 11 kbar in the 'garnet-present' field contributing slab melt to the mantle. These conditions are in agreement with the high *T*/high *P* features of the RBb including: (1) the regional scale extent of the 2.69–2.66 Ga plutons; (2) the moderate HREE contents ($HREE_N$ = 10–177); and (3) ubiquitous presence of rutile needles in quartz throughout the intrusions (Sato and Santosh 2007).

Exsolution in plagioclase (in enderbite) and clinopyroxene (in entrained autoliths) as well as a variable Eu anomaly is evidence for very slow cooling following crystallization. Because charnockitic magmas are anhydrous and lack buoyancy, the accumulated crystal mush may rise slowly and ascend diapirically through the crust (Ashwal 1993; Bolle et al. 2000). Fractional crystallization during magma generation created a cumulate-type intrusion. Early crystallization products were ultramafic (orthopyroxene–clinopyroxene–plagioclase), whereas later more differentiated products were biotite and biotite–hornblende granite and granodiorite, a feature common to the sanukitoid suite (Laurent et al. 2014). The transition from dry to hydrated granitoid rocks is known to be complex due to fluids and heat involved in open system processes during magma ascent (Frost and Frost 2008) and therefore, does not preserve a typical layered intrusion.

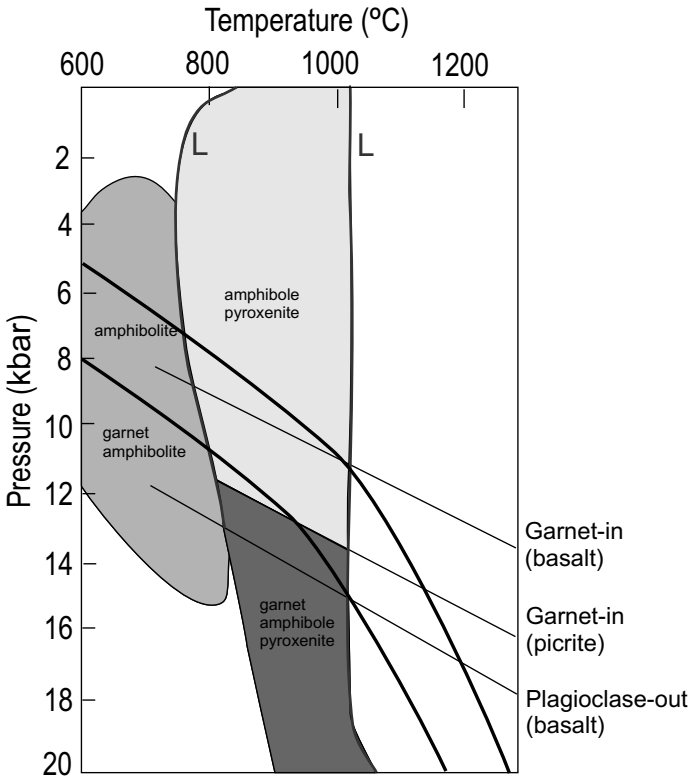

Figure 12. Two typical Archean geotherms for a down-going oceanic slab in an Archean subduction zone after Foley (2008). Amphibolite slab melting in the garnet-present field contributes to the intrusion of a ca. 2.73–2.71 Ga TTG-type crust. Melting of a garnet–amphibole pyroxenite slab contributes slab melts to the mantle to generate a ca. 2.69–2.66 Ga sanukitoid suite.

Regional Correlations

Giant high grade Neoarchean terranes are commonly exposed within the Superior Province, occurring at the margins of the craton or between granite–greenstone terranes (Percival et al. 1992). The Pikwitonei Granulite domain of the northwest Superior Province exposes anhydrous granulite intrusions that formed in the Mesoarchean (3.4–3.0 Ga) and Neoarchean (2.72–2.64 Ga). These lithologies were affected by a multistage metamorphic history at ca. 2716, 2694, 2680 and 2643 Ma, of which the generation of zircon at 2694 and 2680 Ma corresponds to amphibolite- and granulite-facies metamorphism, respectively (Heaman et al. 2011). Large scale Neoarchean plutons similar to those observed in the RBb have also been identified across Hudson Bay, in the Minto block of the northern Superior Province (Bédard 2003). The Minto block is host to Meso–Neoarchean amphibolite- to granulite-facies TTG gneiss, intruded by enderbite and granitoid plutons (Bédard 2003). These intrusions are also similar to those iden-

tified in the Baltic Shield, where a range of dehydrated to hydrated plutons intrude older gneisses and are host to ultramafic xenoliths (e.g. Lobach-Zhuchenko et al. 2005).

Based on a compilation of data from high grade terranes in the Superior Province including the Pikwitonei, Minto block, Split Lake block, Quetico, English River and Opatica domains, Heaman et al. (2011) demonstrated that Neoarchean magmatism and high grade (high *T*/low–moderate *P*) multi-stage metamorphism follows the development of 2.8–2.7 Ga granite–greenstone belts. Furthermore, Whalen et al. (2004) demonstrated that a compositional continuum exists between Neoarchean monzogranite to granodiorite plutonism and sanukitoid plutonism within the Superior Province, indicating that felsic granitoid rocks may be petrogenetically linked to mantle-derived magmatism. Therefore, crustal formation mechanisms in the RBb were synchronous and similar to those occurring in the Superior Province.

Neoarchean high grade igneous terranes have only been briefly described within the Rae craton as exemplified by the granulite domain of Boothia Peninsula mainland (Ryan et al. 2009). In this area, two pulses of magmatism are prominent at ca. 2.66 and 2.61–2.59 Ga, the second pulse being coeval with granulite-facies metamorphism and the intrusion of high-K granite (Hinchey et al. 2011). Here we demonstrate, however, that Neoarchean magmatism in the adjacent RBb spans a continuous time period from 2.73 to 2.66 Ga, with granulite-facies metamorphism being coeval with the intrusion of, and localized to lithologies surrounding, the ca. 2.69–2.66 Ga sanukitoid suite (see also LaFlamme et al. 2014b). Presently, there is no evidence for a 2.60 Ga metamorphic overprint within the RBb.

Implications for Neoarchean Magmatism

Subduction in the late Archean was likely unstable and not comparable to modern day subduction (see Bédard et al. 2013); however, it is the accepted geodynamic setting in which the petrographically variable Neoarchean lithologies (i.e. moderate to high pressure TTGs, sanukitoid intrusions, high-K granite) were formed (Laurent et al. 2014). Alternative mechanisms for the formation of Archean lithologies do exist but remain untested (see Bédard 2006). Conversely, many investigations lend support to the probability of Archean (especially in the Neoarchean) subduction. For instance, Hynes (2014) modelled mantle melting and the cooling of oceanic plates to determine that the resulting negative buoyancy of a subducting slab was in fact strong enough to initiate and sustain subduction in the warmer Archean era. Therefore, assuming subduction of oceanic crust was the mechanism by which Neoarchean TTG-type crust was generated (Smithies et al. 2003; Martin et al. 2005, 2010; see also Bédard 2006 and references therein), the Neoarchean marks a time when the Earth's thermal regime was high enough to induce melting of subducted oceanic crust, but was sufficiently low to generate small amounts of slab melts that were entirely consumed by hybridization with the overlying mantle wedge (e.g. Martin et al. 2005, 2010).

The phenomenon of mantle-derived, sanukitoid magmatism following the formation of granite–greenstone and TTG terranes is common in most Archean cratons worldwide (e.g. Dharwar craton, Moyen et al. 2001; Kalahari craton, Zeh et al. 2009; Fennoscandian Shield, Heilimo et al. 2013; Baltic Shield, Lobach-Zhuchenko et al. 2005, etc.; see Fig. 10). In many cases, the intrusion of regional-scale sanukitoid and high-K plutons occurred within tens of millions of years of the intrusion of TTG gneiss, and developed from a mixture of mantle and recycled crustal components (e.g. Lobach-Zhuchenko et al. 2008; Heilimo et al. 2013). This process is similar to A-type magmatism following subduction in post-Archean convergent plate margins (e.g. Turner et al. 1992; Laurent et al. 2014).

LaFlamme et al. (2014a, b) has demonstrated that Neoarchean magmatism occurred over ~ 63 m.y. within the RBb, between 2.73 and 2.66 Ga. Hafnium isotopic data and zircon geochemical compositions were used to distinguish between the two generations of magmatism. An earlier generation of magmatism formed granitoid gneiss, derived from a ca. 3.25–3.10 Ga mafic crustal substrate, and a later generation of magmatism was derived from a metasomatized primitive mantle that interacted with older crust. A prolonged period of magmatism in "modern style" plate tectonic collisional processes (e.g. Condie and Kröner 2008) is known to have occurred in post-Archean collisional orogens (e.g. Trans-Hudson, Grenville orogens). Similarly, plutonism has been shown to occur coevally with Archean craton-scale deformation and crustal thickening (e.g. Boily et al. 2009; Windley and Garde 2009). Based on Archean seismic reflection patterns, van der Velden et al. (2006) demonstrated that Neoarchean cratons are products of rigid plate behaviour much like in Proterozoic and Phanerozoic orogens, and therefore, behaved in a similar manner during plate collision.

Sanukitoid magmatism has been interpreted to occur following a period of TTG generation (Heilimo et al. 2011) in a style similar to anorogenic magmatism that follows subduction in a collisional environment (Manikyamba et al. 2012). Sanukitoid magmatism is interpreted to be generated by rifting and mantle upwelling related to slab break-off (e.g. Stevenson et al. 1999; Lobach-Zhuchenko et al. 2008; Heilimo et al. 2010). In the RBb, this observation is consistent with a period of magma generation at 2.73–2.71 Ga, followed by voluminous sanukitoid magmatism with negative Ta and Nb anomalies and a coincident depletion in Ti, Y, Yb concentrations in the RBb. Fractional crystallization of magma during slow ascent left behind large cumulate bodies resulting in differentiated anhydrous and hydrous granitoid plutons with entrained websterite and gabbroic xenoliths. Slow magmatic ascent coupled with significant differentiation has been described in Proterozoic orogens as resulting from the removal of an overthickened lithosphere following collapse of an orogen. Subsequent mantle-derived magmas evolved slowly at high *P* before ascending into the crust (McLelland et al. 2010). A similar setting is proposed for the generation of Neoarchean magmas in the RBb (Fig. 13).

Cratonization and Speculations on Kimberlite Emplacement

Globally, Neoarchean granitoid rocks came at a time that documented final stability of a crust that had previously undergone a high rate of recycling (e.g. Hawkesworth et al. 2010). A succession of melts resulted in chemical differentiation of the continental crust, and a change from an amphibolitic to a granulitic lower to middle crust (e.g. Fyfe 1973; Ivanic et al. 2012).

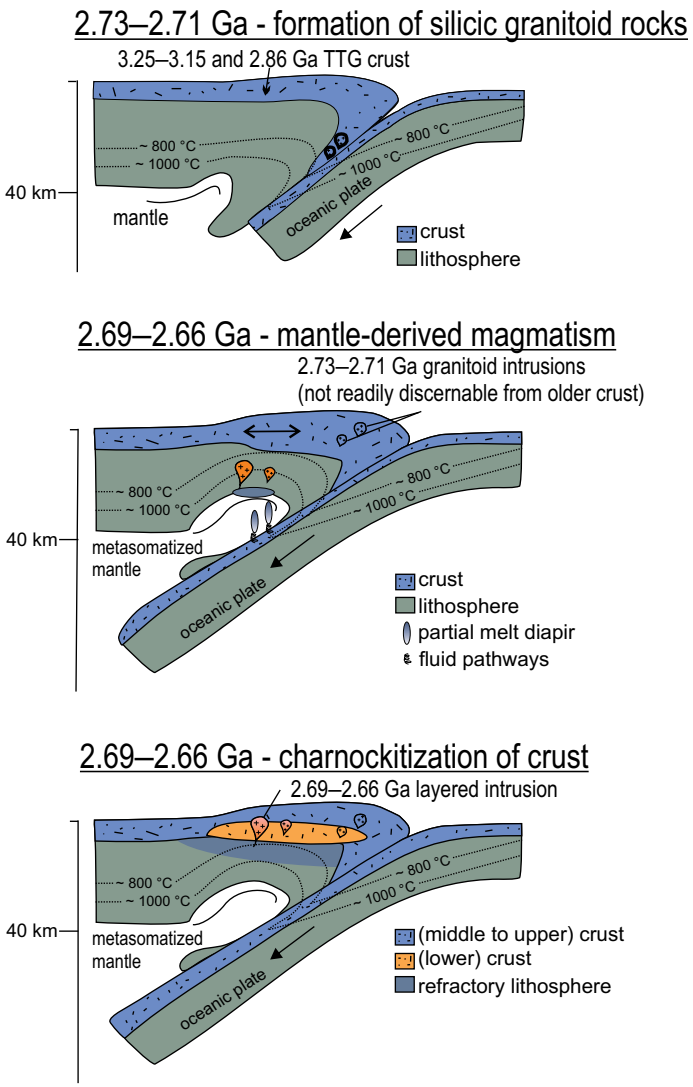

Figure 13. Tectonic setting of sanukitoid generation in the Repulse Bay block. Subduction-driven TTG generation at ca. 2.73–2.71 Ga. Extension, related to an over-thickened lithosphere at 2.69–2.66 Ga, drove mantle-derived magmatism. Colours correlate with the geological map depicted in Figure 2. Neoarchean subduction geotherms after Foley (2008).

The lower crust exposed in the central and southern portion of the RBb demonstrates a bull's eye pattern consisting of pyroxene-bearing ca. 2.73 Ga gneiss that surround the ca. 2.69 Ga dehydrated plutons (see Fig. 2). In these rocks orthopyroxene occurs as the product of a prograde reaction replacing biotite. Therefore, the generation of large volumes of charnockitic magma from a metasomatized depleted upper mantle left behind a granulitic crust and a refractory mantle that helped to stabilize a lithospheric keel in the Neoarchean. The subcontinental lithospheric mantle represents residues and/or cumulates from a high degree of melting at significant depths (e.g. Stevenson et al. 1999; Griffin et al. 2003) and, together with the melt-depleted lower to middle crust, is an important element in cratonization (Shirey et al. 2009). Therefore, voluminous Neoarchean dehydrated plutons may be indicative of an anomalously thick lithospheric keel.

Kimberlite emplacement requires a number of conditions: 1) a tectonically stable craton for at least 500 m.y. with a thick lithospheric keel (e.g. Pasteris 1984); 2) earlier extensive volcanism and/or intrusive magmatism and the addition of K, F, and S to the mantle by metasomatic processes (likely during subduction; e.g. Mitchell 1986; Harte et al. 1987; Shirey et al. 2013); and 3) an asthenospheric source component (Paton et al. 2009). This study suggests that Archean tectonic processes that resulted in fertilization and modification of the subcontinental lithospheric mantle and subsequent cratonization, may also have been critical in generating the perfect conditions for later kimberlite emplacement. Because sanukitoid magmatism occurs in ancient subduction zone settings, its presence may potentially be used as a tool to delineate ancient cratonic margins that have thick and metasomatized lithospheric keels. This statement is in agreement with the fact that the RBb is host to the largest kimberlite pipe in the eastern Canadian Arctic, which is situated proximal to sanukitoid magmatism.

CONCLUSIONS

Neoarchean magmatism in the RBb formed as regional scale ca. 2.73–2.71 Ga TTG-type plutonism and as ca. 2.69–2.66 Ga charnockite, enderbite and granitoid intrusions, host to websterite xenoliths. Based on the similar mineralogical assemblages, whole rock chemical composition of the 2.69–2.66 Ga granitoid intrusions and xenoliths, and similar trace element patterns of pyroxene, the lithologies are interpreted to be coeval and related in part by fractional crystallization. The mantle-like signature (high LILE, Mg#, MgO, Ni, Co) of the ca. 2.69–2.66 Ga lithologies are interpreted to indicate that Neoarchean magmatism was derived from partial melting of a primitive mantle source that was metasomatized by oceanic slab melts. Further crustal contamination occurred by way of interaction with lower crustal melts during magma generation and ascent, accounting for the geochemical and isotopic nature. Based on their chemical composition, the granitoid rocks and autoliths are interpreted to have intruded as a sanukitoid suite.

Neoarchean mantle-derived sanukitoid magmatism in the RBb, followed a period of TTG magmatism at 2.73–2.71 Ga in a subduction zone setting. Similar to post-Archean orogenesis, mantle-derived magmatism resulted from extension related to lithospheric removal beneath an over-thickened crust at depths of 35–40 km. The more buoyant felsic to intermediate anhydrous magmatism rose diapirically as a crystal mush to the middle crust. Sanukitoid magmatism in this region is unique in its preservation as a large scale cumulate intrusion ranging from ultramafic to felsic in composition. The formation of regional scale granulite in conjunction with granulite-facies metamorphism was integral in stabilizing a thick lithospheric keel beneath the RBb.

ACKNOWLEDGEMENTS

This research was funded by the Geological Survey of Canada under the Geomapping for Energy and Minerals program, and an NSERC Discovery Grant to C.R.M.M. Work was carried out as part of a Ph.D. thesis by the first author at the University of New Brunswick. Douglas Hall from the UNB Microscopy and Microanalysis Facility is thanked for help during major element data collection. Cliff Shaw is thanked for offering guidance on an earlier version of this paper. We are grateful to the Editor Brendan Murphy for insightful suggestions and to two anonymous reviewers for thorough and very helpful reviews.

REFERENCES

Ashwal, L.D., 1993, Anorthosites: Springer-Verlag, Berlin, 422 p., http://dx.doi.org/10.1007/978-3-642-77440-9.

Bédard, J.H., 2003, Evidence for regional-scale, pluton-driven, high-grade metamorphism in the Archaean Minto block, northern Superior Province, Canada: The Journal of Geology, v. 111, p. 183–205, http://dx.doi.org/10.1086/345842.

Bédard, J.H., 2006, A catalytic delamination-driven model for coupled genesis of Archean crust and sub-continental lithospheric mantle: Geochimica et Cosmochimica Acta, v. 70, p. 1188–1214, http://dx.doi.org/10.1016/j.gca.2005.11.008.

Bédard, J.H., Harris, L.B., and Thurston, P.C., 2013, The hunting of the snArc: Precambrian Research, v. 229, p. 20–48, http://dx.doi.org/10.1016/j.precamres.2012.04.001.

Berman, R.G., 2010, Metamorphic map of the western Churchill Province, Canada: Geological Survey of Canada Open File, 5279, 55 p., scale 1:2,500,000, http://dx.doi.org/10.4095/287320.

Berman, R.G., Sanborn-Barrie, M., Stern, R.A., and Carson, C.J., 2005, Tectonometamorphism at ca., 2.35 and 1.85 Ga in the Rae domain, Western Churchill Province, Nunavut, Canada: insights from structural, metamorphic and in situ geochronological analysis of the southwestern Committee Bay belt: The Canadian Mineralogist, v. 43, p. 409–442, http://dx.doi.org/10.2113/gscanmin.43.1.409.

Bethune, K.M., and Scammell, R.J., 2003, Geology, geochronology, and geochemistry of Archean rocks in the Eqe Bay area, north-central Baffin Island, Canada: constraints on the depositional and tectonic history of the Mary River Group of northeeastern Rae Province: Canadian Journal of Earth Sciences, v. 40, p. 1137–1167, http://dx.doi.org/10.1139/e03-028.

Bleeker, W., 2003, The late Archean record: a puzzle in ca. 35 pieces: Lithos, v. 71, p. 99–134, http://dx.doi.org/10.1016/j.lithos.2003.07.003.

Boily, M., Leclair, A., Maurice, C., Bédard, J.H., and David, J., 2009, Paleo- to Mesoarchean basement recycling and terrane definition in the northeastern Superior Province, Québec, Canada: Precambrian Research, v. 168, p. 23–44, http://dx.doi.org/10.1016/j.precamres.2008.07.009.

Bolle, O., Diot, H., and Duchesne, J.-C., 2000, Magnetic fabric and deformation in charnockitic igneous rocks of the Bjerkreim–Sokndal layered intrusion (Rogaland, Southwest Norway): Journal of Structural Geology, v. 22, p. 647–667, http://dx.doi.org/10.1016/S0191-8141(99)00183-2.

Brey, G.P., and Köhler, T., 1990, Geothermobarometry in four-phase lherzolites II. New thermobarometers, and practical assessment of existing thermobarometers: Journal of Petrology, v. 31, p. 1353–1378, http://dx.doi.org/10.1093/petrology/31.6.1353.

Condie, K.C., and Kröner, A., 2008, When did plate tectonics begin? Evidence form the geological record, *in* Condie, K.C., and Pease, V., *eds.,* When Did Plate Tectonics Begin on Planet Earth?: Geological Society of America Special Papers, v. 440, p. 281–294, http://dx.doi.org/10.1130/2008.2440(14).

Corrigan, D., Nadeau, L., Brouillette, P., Wodicka, N., Houlé, M.G., Tremblay, T., Machado, G., and Keating, P., 2013, Overview of the GEM Multiple Metals - Melville Peninsula project, central Melville Peninsula, Nunavut: Geological Survey of Canada, Current Research 2013-19, 17 p., http://dx.doi.org/10.4095/292862.

Davis, D.W., Amelin, Y., Nowell, G.M., and Parrish, R.R., 2005, Hf isotopes in zircon from the western Superior province, Canada: Implications for Archean crustal development and evolution of the depleted mantle reservoir: Precambrian Research, v. 140, p. 132–156, http://dx.doi.org/10.1016/j.precamres.2005.07.005.

Davis, W.J., Hanmer, S., Tella, S., Sandeman, H.A., and Ryan, J.J., 2006, U–Pb geochronology of the MacQuoid supracrustal belt and Cross Bay plutonic complex: Key components of the northwestern Hearne Subdomain, western Churchill Province, Nunavut, Canada: Precambrian Research, v. 145, p. 53–80, http://dx.doi.org/10.1016/j.precamres.2005.11.016.

de Hoog, J.C.M., Gall, L., and Cornell, D.H., 2010, Trace-element geochemistry of mantle olivine and application to mantle petrogenesis and geothermobarometry: Chemical Geology, v. 270, p. 196–215, http://dx.doi.org/10.1016/j.chemgeo.2009.11.017.

de Oliveira, M.A., Dall'Agnol, R., Althoff, F.J., and da Silva Leite, A.A., 2009, Mesoarchean sanukitoid rocks of the Rio Maria Granite-Greenstone Terrane, Amazonian craton, Brazil: Journal South American Earth Sciences, v. 27, p. 146–160, http://dx.doi.org/10.1016/j.jsames.2008.07.003.

de Oliveira, M.A., Dall'Agnol, R., and de Almeida, J.A.C., 2011, Petrology of the Mesoarchean Rio Maria Suite and the discrimination of sanukitoid series: Lithos, v. 127, p. 192–209, http://dx.doi.org/10.1016/j.lithos.2011.08.017.

Deer, W., Howie, R.A., and Zussman, J., 1992, An Introduction to the Rock-Forming Minerals (2 edition): Longman, London, 696 p.

DePaolo, D.J., 1981, Neodymium isotopes in the Colorado Front Range and crust-mantle evolution in the Proterozoic: Nature, v. 291, p. 193–196, http://dx.doi.org/10.1038/291193a0.

Drummond, M.S., and Defant, M.J., 1990, A model for trondhjemite-tonalite-dacite genesis and crustal growth via slab melting: Archean to modern comparisons: Journal of Geophysical Research, v. 95, p. 21503–21521, http://dx.doi.org/10.1029/JB095iB13p21503.

Foley, S., 2008, A trace element perspective on Archean crust formation and on the presence or absence of Archean subduction, *in* Condie, K.C., and Pease, V., *eds.,* When Did Plate Tectonics Begin on Planet Earth?: Geological Society of America Special Papers, v. 440, p. 31–50, http://dx.doi.org/10.1130/2008.2440(02).

Frisch, T., 2000, Precambrian geology of Ian Calder Lake, Cape Barclay, and part of Darby Lake map areas, south-central Nunavut: Geological Survey of Canada Bulletin, v. 542, 51 p.

Frost, B.R., and Frost, C.D., 2008, On charnockites: Gondwana Research, v. 13, p. 30–44, http://dx.doi.org/10.1016/j.gr.2007.07.006.

Frost, B.R., Barnes, C.G., Collins, W.J., Arculus, R.J., Ellis, D.J., and Frost, C.D., 2001, A geochemical classification for granitic rocks: Journal of Petrology, v. 42, p. 2033–2048, http://dx.doi.org/10.1093/petrology/42.11.2033.

Fyfe, W.S., 1973, The granulite facies, partial melting and the Archaean crust: Philosophical Transactions of the Royal Society of London, v. 273, p. 457–461, http://dx.doi.org/10.1098/rsta.1973.0011.

Griffin, W.L., O'Reilly, S.Y., Abe, N., Aulbach, S., Davies, R.M., Pearson, N.J., Doyle, B.J., and Kivi, K., 2003, The origin and evolution of Archean lithospheric mantle: Precambrian Research, v. 127, p. 19–41, http://dx.doi.org/10.1016/S0301-9268(03)00180-3.

Griffin, W.L., O'Reilly, S.Y., Afonso, J.C., and Begg, G.C., 2009, The composition and evolution of lithospheric mantle: a re-evaluation and its tectonic implications: Journal of Petrology, v. 50, p. 1185–1204. http://dx.doi.org/10.1093/petrology/egn033.

Halla, J., 2005, Late Archean high-Mg granitoids (sanukitoids) in the southern Karelian domain, eastern Finland; Pb and Nd isotopic constraints on crust-mantle interactions: Lithos, v. 79, p. 161–178, http://dx.doi.org/10.1016/j.lithos.2004.05.007.

Halla, J., van Hunen, J., Heilimo, E., and Hölttä, P., 2009, Geochemical and numerical constraints on Neoarchean plate tectonics: Precambrian Research, v. 174, p. 155–162, http://dx.doi.org/10.1016/j.precamres.2009.07.008.

Harte, B., Winterburn, P.A., and Gurney, J.J., 1987, Metasomatic phenomena in garnet peridotite facies mantle xenoliths from the Matsoku kimberlite pipe, Lesotho, *in* Menzies, M.A., and Hawkesworth, C.J., *eds.*, Mantle Metasomatism: Academic Press, London, p. 145–220.

Hartlaub, R.P., Chacko, T., Heaman, L.M., Creaser, R.A., Ashton, K.E., and Simonetti, T., 2005, Ancient (Meso- to Paleoarchean) crust in the Rae Province, Canada: Evidence from Sm–Nd and U–Pb constraint: Precambrian Research, v. 141, p. 137–153, http://dx.doi.org/10.1016/j.precamres.2005.09.001.

Hawkesworth, C.J., Dhuime, B., Pietranik, A.B., Cawood, P.A., Kemp, A.I.S., and Storey, C.D., 2010, The generation and evolution of the continental crust: Journal of the Geological Society, v. 167, p. 229–248, http://dx.doi.org/10.1144/0016-76492009-072.

Heaman, L.M., Böhm, Ch.O., Machado, N., Krogh, T.E., Weber, W., and Corkery, M.T., 2011, The Pikwitonei Granulite Domain, Manitoba: a giant Neoarchean high-grade terrane in the northwest Superior Province: Canadian Journal of Earth Sciences, v. 48, p. 205–245, http://dx.doi.org/10.1139/E10-058.

Heilimo, E., Halla, J., and Hölttä, P., 2010, Discrimination and origin of the sanukitoid series: Geochemical constraints from the Neoarchean western Karelian Province (Finland): Lithos, v. 115, p. 27–39, http://dx.doi.org/10.1016/j.lithos.2009.11.001.

Heilimo, E., Halla, J., and Huhma, H., 2011, Single-grain zircon U–Pb age constraints of the western and eastern sanukitoid zones in the Finnish part of the Karelian Province: Lithos, v. 121, p. 87–99, http://dx.doi.org/10.1016/j.lithos.2010.10.006.

Heilimo, E., Halla, J., Andersen, T., and Huhma, H., 2013, Neoarchean crustal recycling and mantle metasomatism: Hf–Nd–Pb–O isotope evidence from sanukitoids of the Fennoscandian shield: Precambrian Research, v. 228, p. 250–266, http://dx.doi.org/10.1016/j.precamres.2012.01.015.

Hinchey, A.M., Davis, W.J., Ryan, J.J., and Nadeau, L., 2011, Neoarchean high-potassium granites of the Boothia mainland area, Rae domain, Churchill Province: U–Pb zircon and Sm–Nd whole rock isotopic constraints: Canadian Journal of Earth Sciences, v. 48, p. 247–279, http://dx.doi.org/10.1139/E10-071.

Hoffman, P.F., 1988, United plates of America, the birth of a craton: Early Proterozoic assembly and growth of Laurentia: Annual Review of Earth and Planetary Sciences, v. 16, p. 543–603, http://dx.doi.org/10.1146/annurev.ea.16.050188.002551.

Hynes, A., 2014, How feasible was subduction in the Archean?: Canadian Journal of Earth Sciences, v. 51, p. 286–296, http://dx.doi.org/10.1139/cjes-2013-0111.

Ionov, D.A., Bodinier, J.-L., Mukasa, S.B., and Zanetti, A., 2002, Mechanisms and sources of mantle metasomatism: Major and trace element compositions of peridotite xenoliths from Spitsbergen in the context of numerical modelling: Journal of Petrology, v. 43, p. 2219–2259, http://dx.doi.org/10.1093/petrology/43.12.2219.

Irvine, T.N., and Baragar, W.R.A., 1971, A guide to the chemical classification of the

common volcanic rocks: Canadian Journal of Earth Sciences, v. 8, p. 523–548, http://dx.doi.org/10.1139/e71-055.

Irving, A.J., and Frey, F.A., 1984, Trace element abundances in megacrysts and their host basalts: Constraints on partition coefficients and megacryst genesis: Geochimica et Cosmochimica Acta, v. 48, p. 1201–1221, http://dx.doi.org/10.1016/0016-7037(84)90056-5.

Ivanic, T.J., Van Kranendonk, M.J., Kirkland, C.L., Wyche, S., Wingate, M.T.D., and Belousova, E.A., 2012, Zircon Lu–Hf isotopes and granite geochemistry of the Murchison Domain of the Yilgarn craton: Evidence for reworking of Eoarchean crust during Meo-Neoarchean plume-driven magmatism: Lithos, v. 148, p. 112–127, http://dx.doi.org/10.1016/j.lithos.2012.06.006.

Jenner, G.A., 1996, Trace element geochemistry of igneous rocks: geochemical nomenclature and analytical geochemistry, *in* Wyman, D.A., *ed.*, Trace Element Geochemistry of Volcanic Rocks: Applications for Massive Sulphide Exploration: Geological Association of Canada - Short Course Notes 12, p. 51–77.

Kerrich, R., and Wyman, D., 1996, Trace element systematics: an overview, *in* Wyman, D.A., *ed.,* Trace Element Geochemistry of Volcanic Rocks: Applications for Massive Sulphide Exploration: Geological Association of Canada - Short Course Notes 12, p. 1–50.

Ketchum, J.W.F., Bleeker, W., and Stern, R.A., 2004, Evolution of an Archean basement complex and its autochthonous cover, southern Slave Province, Canada: Precambrian Research, v. 135, p. 149–176, http://dx.doi.org/10.1016/j.precamres.2004.08.005.

LaFlamme, C., McFarlane, C.R.M., and Corrigan, D., 2014a, U–Pb, Lu–Hf and REE in zircon from 3.2 to 2.6 Ga Archean gneisses of the Repulse Bay block, Melville Peninsula, Nunavut: Precambrian Research, v. 252, p. 223–239, http://dx.doi.org/10.1016/j.precamres.2014.07.012.

LaFlamme, C., McFarlane, C.R.M., Corrigan, D., and Wodicka, N., 2014b, Origin and tectonometamorphic history of the Repulse Bay block, Melville Peninsula, Nunavut: exotic terrane or deeper level of the Rae craton?: Canadian Journal of Earth Sciences, v. 51, p. 1097–1122, http://www.nrcresearchpress.com/doi/abs/10.1139/cjes-2014-0040#.VJDVJCvF_Do.

Laurent, O., Martin, H., Doucelance, R., Moyen, J.-F., and Paquette, J.-L., 2011, Geochemistry and petrogenesis of high-K "sanukitoids" from the Bulai pluton, Central Limpopo Belt, South Africa: Implications for geodynamic changes at the Archaean–Proterozoic boundary: Lithos, v. 123, p. 73–91, http://dx.doi.org/10.1016/j.lithos.2010.12.009.

Laurent, O., Doucelance, R., Martin, H., and Moyen, J.-F., 2013, Differentiation of the late-Archaean sanukitoid series and some implications for crustal growth: Insights from geochemical modelling on the Bulai Pluton, Central Limpopo Belt, South Africa: Precambrian Research, v. 227, p. 186–203, http://dx.doi.org/10.1016/j.precamres.2012.07.004.

Laurent, O., Martin, H., Moyen, J.-F., and Doucelance, R., 2014, The diversity and evolution of late-Archean granitoids: Evidence for the onset of "modern-style" plate tectonics between 3.0 and 2.5 Ga: Lithos, v. 205, p. 208–235, http://dx.doi.org/10.1016/j.lithos.2014.06.012.

Lobach-Zhuchenko, S.B., Rollinson, H.R., Chekulaev, V.P., Arestova, N.A., Kovalenko, A.V., Ivanikov, V.V., Guseva, N.S., Sergeev, S.A., Matukov, D.I., and Jarvis, K.E., 2005, The Archaean sanukitoid series of the Baltic Shield: geological setting, geochemical characteristics and implications for their origin: Lithos, v. 79, p. 107–128, http://dx.doi.org/10.1016/j.lithos.2004.04.052.

Lobach-Zhuchenko, S.B., Rollinson, H., Chekulaev, V.P., Savatenkov, V.M., Kovalenko, A.V., Martin, H., Guseva, N.S., and Arestova, N.A., 2008, Petrology of a late Archaean, highly potassic sanukitoid pluton from the Baltic Shield: Insights into late Archaean mantle metasomatism: Journal of Petrology, v. 49, p. 393–420, http://dx.doi.org/10.1093/petrology/egm084.

Ma, X., Guo, J., Liu, F., Qian, Q., and Fan, H., 2013, Zircon U–Pb ages, trace elements, and Nd–Hf isotopic geochemistry of Guyang sanukitoids and related rocks: Implications for the Archean crustal evolution of the Yinshan Block, North China Craton: Precambrian Research, v. 230, p. 61–78, http://dx.doi.org/10.1016/j.precamres.2013.02.001.

Manikyamba, C., Kerrich, R., Polat, A., Raju, K., Satyanarayanan, M., and Krishna, A.K., 2012, Arc picrite-potassic adakitic-shoshonitic volcanic association of the Neoarchean Sigegudda greenstone terrane, western Dharwar craton: Transition from arc wedge to lithosphere melting: Precambrian Research, v. 212–213, p. 207–224, http://dx.doi.org/10.1016/j.precamres.2012.05.006.

Martin, H., and Moyen, J.-F., 2002, Secular changes in tonalite-trondhjemite-granodiorite composition as markers of the progressive cooling of Earth: Geology, v. 30, p. 319–322, http://dx.doi.org/10.1130/0091-7613(2002)030<0319:SCITTG>2.0.CO;2.

Martin, H., Smithies, R.H., Rapp, R., Moyen, J.-F., and Champion, D., 2005, An overview of adakite, tonalite-trondhjemite-granodiorite (TTG), and sanukitoid: relationships and some implications for crustal evolution: Lithos, v. 79, p. 1–24, http://dx.doi.org/10.1016/j.lithos.2004.04.048.

Martin, H., Moyen, J.-F., and Rapp, R., 2010, The sanukitoid series; magmatism at the Archaean–Proterozoic transition, *in* Clemens, J.D., *ed.,* Sixth Hutton Symposium on The Origin of Granites and Related Rocks: Geological Society of America Special Papers, v. 472, p. 15–33, http://dx.doi.org/10.1130/2010.2472(02).

McLelland, J.M., Selleck, B.W., Hamilton, M.A., and Bickford, M.E., 2010, Late- to post-tectonic setting of some major Proterozoic anorthosite-mangerite-charnockite-granite (AMCG) suites: The Canadian Mineralogist, v. 48, p. 729–750, http://dx.doi.org/10.3749/canmin.48.4.729.

Mitchell, R.H., 1986, Kimberlites: Mineralogy, Geochemistry, and Petrology: Springer, New York, 442 p., http://dx.doi.org/10.1007/978-1-4899-0568-0.

Moyen, J.-F., 2011, The composite Archaean grey gneisses: Petrological significance, and evidence for a non-unique tectonic setting for Archaean crustal growth: Lithos, v. 123, p. 21–36, http://dx.doi.org/10.1016/j.lithos.2010.09.015.

Moyen, J.-F., and Stevens, G., 2006, Experimental constraints on TTG petrogenesis: Implications for Archean geodynamics, *in* Benn, K., Mareschal, J.-C., and Condie, K.C., *eds.,* Archean Geodynamics and Environments: American Geophysical Union, Geophysical Monograph Series, v. 164, p. 149–175, http://dx.doi.org/10.1029/164GM11.

Moyen, J.-F., Martin, H., and Jayananda, M., 2001, Multi-element geochemical modelling of crust-mantle interactions during late-Archaean crustal growth; the Closepet Granite (South India): Precambrian Research, v. 112, p. 87–105, http://dx.doi.org/10.1016/S0301-9268(01)00171-1.

Mungall, J.E., 2002, Roasting the mantle: Slab melting and the genesis of major Au and Au-rich Cu deposits: Geology, v. 30, p. 915–918, http://dx.doi.org/10.1130/0091-7613(2002)030<0915:RTMSMA>2.0.CO;2.

Nagel, T.J., Hoffmann, J.E., and Münker, C., 2012, Generation of Eoarchean tonalite-trondhjemite-granodiorite series from thickened mafic arc crust: Geology, v. 40, p. 375–378, http://dx.doi.org/10.1130/G32729.1.

Ohba, T., Matsuoka, K., Kimura, Y., Ishikawa, H., and Fujimaki, H., 2009, Deep crystallization differentiation of arc tholeiite basalt magmas from northern Honshu arc, Japan: Journal of Petrology, v. 50, p. 1025–1046, http://dx.doi.org/10.1093/petrology/egp030.

Pasteris, J.D., 1984, Kimberlites: Complex mantle melts: Annual Review in Earth and Planetary Sciences, v. 12, p. 133–153, http://dx.doi.org/10.1146/annurev.ea.12.050184.001025.

Paton, C., Hergt, J.M., Woodhead, J.D., Phillips, D., and Shee, S.R., 2009, Identifying the asthenospheric component of kimberlite magmas from the Dharwar Craton, India: Lithos, v. 112, p. 296–310, http://dx.doi.org/10.1016/j.lithos.2009.03.019.

Paton, C., Hellstrom, J., Paul, B., Woodhead, J., and Hergt, J., 2011, Iolite: Freeware for the visualisation and processing of mass spectrometric data: Journal of Analytical Atomic Spectrometry, v. 26, p. 2508–2518, http://dx.doi.org/10.1039/c1ja10172b.

Pearce, J.A., 1982, Trace element characteristics of lavas from destructive plate boundaries, *in* Thorpe, R.S., *ed.,* Orogenic andesites and related rocks: John Wiley and Sons, Chichester, England, p. 528–548.

Pearce, J.A., and Norry, M.J., 1979, Petrogenetic implications of Ti, Zr, Y, and Nb variations in volcanic rocks: Contributions to Mineralogy and Petrology, v. 69, p. 33–47, http://dx.doi.org/10.1007/BF00375192.

Percival, J.A., and Mortensen, J.K., 2002, Water-deficient calc-alkaline plutonic rocks of northeastern Superior Province, Canada: significance of charnockitic magmatism: Journal of Petrology, v. 43, p. 1617–1650, http://dx.doi.org/10.1093/petrology/43.9.1617.

Percival, J.A., Mortensen, J.K., Stern, R.A., Card, K.D., and Bégin, N.J., 1992, Giant granulite terranes of northeastern Superior Province: the Ashuanipi complex and Minto block: Canadian Journal of Earth Sciences, v. 29, p. 2287–2308, http://dx.doi.org/10.1139/e92-179.

Peterson, T.D., van Breemen, O., Sandeman, H., and Cousens, B., 2002, Proterozoic (1.85–1.75 Ga) igneous suites of the Western Churchill Province: granitoid and ultrapotassic magmatism in a reworked Archean hinterland: Precambrian Research, v. 119, p. 73–100, http://dx.doi.org/10.1016/S0301-9268(02)00118-3.

Qian, Q., and Hermann, J., 2010, Formation of high-Mg diorites through assimilation of peridotite by monzodiorite magma at crustal depths: Journal of Petrology, v. 51, p. 1381–1416, http://dx.doi.org/10.1093/petrology/egq023.

Qian, Q., and Hermann, J., 2013, Partial melting of lower crust at 10–15 kbar: constraints on adakite and TTG formation: Contributions to Mineralogy and Petrology, v. 165, p. 1195–1224, http://dx.doi.org/10.1007/s00410-013-0854-9.

Rapp, R.P., Norman, M.D., Laporte, D., Yaxley, G.M., Martin, H., and Foley, S.F., 2010, Continent formation in the Archean and chemical evolution of the cratonic lithosphere: Melt-rock reaction experiments at 3–4 GPa and petrogenesis of Archean Mg-diorites (sanukitoids): Journal of Petrology, v. 51, p. 1237–1266, http://dx.doi.org/10.1093/petrology/egq017.

Rayner, N., Chakungal, J., and Sanborn-Barrie, M., 2011, New U–Pb geochronological results from plutonic and sedimentary rocks of Southampton Island, Nunavut: Geological Survey of Canada, Current Research 2011-5, 20 p.,

http://dx.doi.org/10.4095/287286.
Rayner, N., Sanborn-Barrie, M., and Chakungal, J., 2013, A 3.0 to 2.0 Ga plutonic record on Southampton Island, Nunavut: Geological Survey of Canada, Current Research 2013-6, 18 p., http://dx.doi.org/10.4095/292214.
Roach, I.C., 2004, Mineralogy, textures and P-T relationships of a suite of xenoliths from the Monaro Volcanic Province, New South Wales, Australia: Journal of Petrology, v. 45, p. 739–758, http://dx.doi.org/10.1093/petrology/egg108.
Rubatto, D., and Hermann, J., 2003, Zircon formation during fluid circulation in eclogites (Monviso, Western Alps): implications for Zr and Hf budget in subduction zones: Geochimica et Cosmochimica Acta, v. 67, p. 2173–2187, http://dx.doi.org/10.1016/S0016-7037(02)01321-2.
Rudnick, R.L., and Fountain, D.M., 1995, Nature and composition of the continental crust: A lower crustal perspective: Reviews in Geophysics, v. 33, p. 267–309, http://dx.doi.org/10.1029/95RG01302.
Rudnick, R.L., McDonough, W.F., McCulloch, M.T., and Taylor, S.R., 1986, Lower crustal xenoliths from Queensland, Australia: Evidence for deep crustal assimilation and fractionation of continental basalts: Geochimica et Cosmochimica Acta, v. 50, p. 1099–1115, http://dx.doi.org/10.1016/0016-7037(86)90391-1.
Ryan, J.J., Nadeau, L., Hinchey, A.M., James, D.T., Sandeman, H.A., Schetselaar, E.M., and Berman, R.G., 2009, Bedrock geology of the southern Boothia mainland area, Kitikmeot region, Nunavut: Current Research (Paper 2009-1), 21 p.
Sandeman, H.A., Cousens, B.L., and Hemmingway, C.J., 2003, Continental tholeiitic mafic rocks of the Paleoproterozoic Hurwitz Group, Central Hearne subdomain, Nunavut: insight into the evolution of the Hearne sub-continental lithosphere: Canadian Journal of Earth Sciences, v. 40, p. 1219–1237, http://dx.doi.org/10.1139/e03-035.
Sano, S., Oberhänsli, R., Romer, R.L., and Vinx, R., 2002, Petrological, geochemical and isotopic constraints on the origin of the Harzburg Intrusion, Germany: Journal of Petrology, v. 43, p. 1529–1549, http://dx.doi.org/10.1093/petrology/43.8.1529.
Sato, H., 1977, Nickel content of basaltic magmas: identification of primary magmas and a measure of the degree of olivine fractionation: Lithos, v. 10, p. 113–120, http://dx.doi.org/10.1016/0024-4937(77)90037-8.
Sato, K., and Santosh, M., 2007, Titanium in quartz as a record of ultrahigh-temperature metamorphism: the granulites of Karur, southern India: Mineralogical Magazine, v. 71, p. 143–154, http://dx.doi.org/10.1180/minmag.2007.071.2.143.
Schmidberger, S.S., and Francis, D., 1999, Nature of the mantle roots beneath the North American craton: Mantle xenolith evidence from Somerset Island kimberlites, Lithos, v. 48, p. 195–216, http://dx.doi.org/10.1016/S0024-4937(99)00029-8.
Schmidt, M.W., and Poli, S., 1998, Experimentally based water budgets for dehydrating slabs and consequences for arc magma generation: Earth and Planetary Science Letters, v. 163, p. 361–379, http://dx.doi.org/10.1016/S0012-821X(98)00142-3.
Shirey, S.B., and Hanson, G.N., 1984, Mantle-derived Archaean monzodiorites and trachyandesites: Nature, v. 310, p. 222–224, http://dx.doi.org/10.1038/310222a0.
Shirey, S.B., Ayer, J.A., and Wyman, D.A., 2009, Re-Os and PGE systematics of Neoarchean websterite xenoliths and diamondiferous lamprophyres of the Wawa area, Superior Province, Canada (abstract): Eos, Transactions, American Geophysical Union, Fall Meeting 2009, v. 90, Abstract # V13A-2003.
Shirey, S.B., Cartigny, P., Frost, D.J., Keshav, S., Nestola, F., Nimis, Pl, Pearson, D.G., Sobolev, N.V., and Walter, M.J., 2013, Diamonds and the geology of mantle carbon: Reviews in Mineralogy and Geochemistry, v. 75, p. 355–421, http://dx.doi.org/10.2138/rmg.2013.75.12.
Skulski, T., Sandeman, H., Sanborn-Barrie, M., MacHattie, T., Young, M., Carson, C., Berman, R., Brown, J., Rayner, N., Panagapko, D., Byrne, D., and Deyell, C., 2003, Bedrock geology of the Ellice Hills map area and new constraints on the regional geology of the Committee Bay area, Nunavu: Geological Survey of Canada, Current Research 2003-C22, 11 p.
Smithies, R.H., and Champion, D.C., 2000, The Archaean high-Mg diorite suite: Links to tonalite-trondhjemite-granodiorite magmatism and implications for early Archaean crustal growth: Journal of Petrology, v. 41, p. 1653–1671, http://dx.doi.org/10.1093/petrology/41.12.1653.
Smithies, R.H., Champion, D.C., and Cassidy, K.F., 2003, Formation of Earth's early Archaean continental crust: Precambrian Research, v. 127, p. 89–101, http://dx.doi.org/10.1016/S0301-9268(03)00182-7.
Stern, R.A., and Hanson, G.N., 1991, Archean high-Mg granodiorite: A derivative of light rare earth element-enriched monzodiorite of mantle origin: Journal of Petrology, v. 32, p. 201–238, http://dx.doi.org/10.1093/petrology/32.1.201.
Stern, R.A., Hanson, G.N., and Shirey, S.B., 1989, Petrogenesis of mantle-derived, LILE-enriched Archean monzodiorites and trachyandesites (sanukitoids) in southwestern Superior Province: Canadian Journal of Earth Sciences, v. 26, p. 1688–1712, http://dx.doi.org/10.1139/e89-145.
Stevenson, R., Henry, P., and Gariépy, C., 1999, Assimilation-fractional crystallization origin of Archean sanukitoid suites: Western Superior Province, Canada: Precambrian Research, v. 96, p. 83–99, http://dx.doi.org/10.1016/S0301-9268(99)00009-1.
Sun, S.-s., and McDonough, W.F., 1989, Chemical and isotopic systematics of oceanic basalts: implications for mantle composition and processes: Geological Society, London, Special Publications, v. 42, p. 313–345, http://dx.doi.org/10.1144/GSL.SP.1989.042.01.19.
Turner, S., Sandiford, M., and Foden, J., 1992, Some geodynamic and compositional constraints on "postorogenic" magmatism: Geology, v. 20, p. 931–934, http://dx.doi.org/10.1130/0091-7613(1992)020<0931:SGACCO>2.3.CO;2.
van Breemen, O., Pehrsson, S., and Peterson, T.D., 2007, Reconnaissance U–Pb SHRIMP geochronology and Sm–Nd isotope analyses from the Tehery-Wager Bay gneiss domain, western Churchill Province, Nunavut: Geological Survey of Canada, Current Research 2007-F2, 15 p.
van der Velden, A.J., Cook, F.A., Drummond, B.J., and Goleby, B.R., 2006, Reflections of the Neoarchean: A global perspective, *in* Benn, K., Mareschal, J.-C., and Condie, K.C., *eds.,* A Global Perspective in Archean Geodynamics and Environments: American Geophysical Union Geophysical Monograph Series, v. 164, p. 255–265, http://dx.doi.org/10.1029/164GM16.
Walter, M.J., 2003, Melt extraction and compositional variability in mantle lithosphere, *in* Holland, H.D., and Turekian, K.K., *eds.,* Treatise on Geochemistry: Volume 2: The Mantle and Core: Elsevier, p. 363–394, http://dx.doi.org/10.1016/B0-08-043751-6/02008-9.
Whalen, J.B., Percival, J.A., McNicoll, V.J., and Longstaffe, F.J., 2004, Geochemical and isotopic (Nd–O) evidence bearing on the origin of late- to post-orogenic high-K granitoid rocks in the Western Superior Province: implications for late Archean tectonomagmatic processes: Precambrian Research, v. 132, p. 303–326, http://dx.doi.org/10.1016/j.precamres.2003.11.007.
Whitney, D.L., and Evans, B.W., 2010, Abbreviations for names of rock-forming minerals: American Mineralogist, v. 95, p. 185–187, http://dx.doi.org/10.2138/am.2010.3371.
Windley, B.F., and Garde, A.A., 2009, Arc-generated blocks with crustal sections in the North Atlantic craton of West Greenland: Crustal growth in the Archean with modern analogues: Earth-Science Reviews, v. 93, p. 1–30, http://dx.doi.org/10.1016/j.earscirev.2008.12.001.
Wyllie, P.J., and Sekine, T., 1982, The formation of mantle phlogopite in subduction zone hybridization: Contributions to Mineralogy and Petrology, v. 79, p. 375–380, http://dx.doi.org/10.1007/BF01132067.
Zaleski, E., Davis, W.J., and Sandeman, H.A., 2001, Continental extension, mantle magmas and basement/cover relationships: Record - Australian Geological Survey Organisation 2001/37, p. 374–376.
Zeh, A., Gerdes, A., and Barton, J.M., Jr., 2009, Archean accretion and crustal evolution of the Kalahari Craton—the zircon age and Hf isotope record of granitic rocks from Barberton/Swaziland to the Francistown arc: Journal of Petrology, v. 50, p. 933–966, http://dx.doi.org/10.1093/petrology/egp027.

Received August 2014
Accepted as revised November 2014
First published on the web December 2014

Appendix 1: Location of samples used for analysis.

Sample	Easting[a]	Northing[a]
10CXAD003	643251.8	7383655.7
10CXAL001	643251.8	7383655.7
10CXAL118	631908.2	7413757.5
10CXAL131	638853.8	7394339.6
10CXAL134	639402.2	7390775.2
10CXAL184	681910.8	7393372.8
10CXAL190	652515.0	7385280.6
10CXAL249	545100.0	7370000.0
10CXAN031	697030.7	7394330.8

[a] NAD 1983; UTM Zone 16N

Appendix 2: Trace element geochemistry in pyroxene occurring in Archean enderbite and ultramafic autoliths reported in ppm.

Sample	Si	2SE	Ca	2SE	Y	2SE	Zr	2SE	Nb	2SE	La	2SE	Ce	2SE	Nd	2SE	Sm	2SE
10CXAL134B (UTM 639402.2E, 7390775.2N)																		
websterite xenolith in ca. 2.67 Ga enderbite																		
opx1	282000	1600	3400	180	2.09	0.04	0.28	0.02	0.013	0.003	0.214	0.025	0.484	0.045	0.42	0.04	0.14	0.02
cpx1b	242000	1100	149250	920	88.11	0.43	28.67	0.27	0.152	0.007	22.9	0.95	111	1.7	103.2	0.5	27.28	0.18
cpx2	240000	1000	161000	2000	70.66	0.85	32.25	0.40	0.024	0.003	16.26	0.35	78.84	0.97	71.9	0.9	19.64	0.27
opx2b	264000	1600	5110	160	3.60	0.08	0.73	0.03	0.027	0.004	0.677	0.082	2.11	0.15	1.60	0.09	0.44	0.03
opx3	266000	2200	3101	71	2.52	0.03	0.41	0.02	0.004	0.001	0.037	0.017	0.106	0.038	0.12	0.02	0.07	0.01
opx3b	267000	1700	2851	99	2.32	0.04	0.50	0.02	0.006	0.002	0.138	0.013	0.251	0.024	0.26	0.03	0.10	0.01
cpx4	244000	1100	159000	1100	83.59	0.53	31.9	0.29	0.057	0.005	19.1	0.31	95.74	0.65	90.9	0.4	24.53	0.19
opx4b	265000	1600	2960	110	2.46	0.03	0.31	0.08	0.005	0.001	0.094	0.022	0.35	0.11	0.18	0.03	0.08	0.01
cpx5	234880	680	146260	920	67.27	0.33	26.0	1.10	0.125	0.006	20.55	0.73	90.9	1.3	80.3	0.54	20.60	0.13
10CXAL190A (UTM 652515.0E, 7385280.6N; U-Pb concordant age: 2670 ± 11 Ma)																		
Orthopyroxene-clinopyroxene-biotite enderbite																		
opx1	250000	2500	4640	150	16.25	0.08	0.55	0.05	9.06	0.11	1.524	0.068	3.33	0.15	1.59	0.07	0.46	0.03
cpx1b	212000	1100	13960	280	13.64	0.22	0.28	0.02	17.2	2.2	3.77	0.18	7.02	0.52	3.73	0.12	1.17	0.07
cpx2	181000	2500	13300	2100	18.45	0.20	0.40	0.04	0.056	0.010	7.5	2.5	12.60	4.00	5.1	1.3	1.04	0.16
opx2b	270000	1400	4870	130	16.22	0.12	0.20	0.01	0.008	0.002	0.703	0.085	1.34	0.12	0.70	0.05	0.32	0.02
opx3	269000	1400	4880	110	16.68	0.12	0.36	0.03	0.016	0.003	0.284	0.013	0.78	0.03	0.59	0.04	0.36	0.03
opx3b	270000	3300	5380	210	14.90	0.09	0.24	0.01	0.005	0.002	1.262	0.087	2.07	0.11	0.90	0.05	0.33	0.02
opx4	249000	2000	5560	160	15.84	0.10	0.19	0.01	0.033	0.004	0.246	0.013	0.57	0.04	0.39	0.04	0.29	0.02
cpx4b	188000	1700	24540	520	13.45	0.15	0.13	0.02	0.027	0.006	14	1.1	16.20	1.20	6.66	0.47	1.17	0.07
opx5b	249000	1400	4480	140	17.85	0.24	0.20	0.01	0.004	0.001	0.393	0.045	0.90	0.07	0.5	0.04	0.23	0.02

Appendix 2: continued

Sample	Eu	2SE	Gd	2SE	Dy	2SE	Er	2SE	Yb	2SE	Th	2SE	U	2SE
10CXAL134B (UTM 639402.2E, 7390775.2N)														
websterite xenolith in ca. 2.67 Ga enderbite														
opx1	0.009	0.003	0.16	0.02	0.29	0.01	0.29	0.02	0.57	0.03	0.025	0.004	0.025	0.003
cpx1b	1.471	0.018	23.90	0.17	19.25	0.12	8.71	0.08	6.75	0.07	0.650	0.140	0.187	0.014
cpx2	1.206	0.029	17.80	0.28	15.36	0.22	7.27	0.10	5.87	0.11	0.084	0.022	0.088	0.004
opx2b	0.032	0.005	0.45	0.02	0.57	0.02	0.50	0.02	0.79	0.03	0.044	0.006	0.025	0.003
opx3	0.007	0.002	0.13	0.01	0.32	0.02	0.39	0.02	0.79	0.03	0.003	0.002	0.002	0.001
opx3b	0.014	0.003	0.13	0.02	0.29	0.02	0.34	0.01	0.68	0.02	0.002	0.001	0.005	0.001
cpx4	1.403	0.027	21.91	0.21	18.12	0.14	8.40	0.09	6.71	0.08	0.156	0.020	0.108	0.004
opx4b	0.009	0.002	0.15	0.01	0.31	0.01	0.37	0.01	0.77	0.03	0.017	0.008	0.011	0.002
cpx5	1.261	0.019	17.71	0.14	14.54	0.10	6.73	0.07	5.37	0.05	0.453	0.098	0.155	0.012
10CXAL190A (UTM 652515.0E, 7385280.6N; U-Pb concordant age: 2670 ± 11 Ma)														
Orthopyroxene-clinopyroxene-biotite enderbite														
opx1	0.030	0.004	0.84	0.04	2.42	0.06	2.59	0.04	3.99	0.07	-	-	0.013	0.005
cpx1b	0.076	0.011	1.44	0.09	2.37	0.06	2.03	0.06	2.85	0.09	-	-	0.004	0.001
cpx2	0.079	0.024	1.37	0.15	2.78	0.08	2.95	0.05	3.82	0.12	-	-	0.003	0.002
opx2b	0.021	0,003	0.71	0.03	2.44	0.05	2.63	0.04	3.95	0.06	-	-	-	-
opx3	0.019	0.002	0.73	0.04	2.41	0.04	2.66	0.04	3.97	0.07	-	-	-	-
opx3b	0.025	0.004	0.67	0.05	2.09	0.04	2.38	0.04	3.75	0.07	-	-	-	-
opx4	0.020	0.004	0.72	0.03	2.36	0.05	2.49	0.04	3.99	0.07	-	-	-	-
cpx4b	0.116	0.010	1.33	0.05	2.16	0.04	1.97	0.06	2.99	0.07	-	-	0.003	0.001
opx5b	0.025	0.004	0.63	0.04	2.43	0.05	2.86	0.07	4.43	0.09	-	-	-	-

Appendix 3: Trace element geochemistry in olivine reported in ppm.

Sample	Li	2SE	Na	2SE	Al	2SE	P	2SE	Ca	2SE	Sc	2SE	Ti	2SE	V	2SE	Cr	2SE
10CXAL249 (UTM 545100.0E, 7370000.0N)																		
dunite xenolith in ca. 2.72 Ga granitoid gneiss																		
L249_1	3.35	0.63	-	-	12.6	2.6	8.4	5.1	480	340	17.33	0.27	11.3	1.3	1.60	0.31	530	100
L249_2	4.95	0.51	48	18	5.6	1.5	24.7	5.9	540	350	16.59	0.32	9.1	1.1	0.28	0.09	36	16
L249_3	3.19	0.66	710	110	65.5	7.0	24.2	6.3	460	430	15.97	0.34	10.9	1.6	1.17	0.30	318	94
L249_4	2.82	0.72	-	-	2.0	1.1	11.5	6.6	310	370	15.31	0.30	7.5	1.5	0.17	0.08	24	5
L249_5	3.47	0.84	-	-	1.8	0.9	14.8	6.2	320	440	14.82	0.33	6.9	1.5	0.22	0.08	23	8
L249_6	3.85	0.63	-	-	1.1	1.1	19.8	5.3	660	390	13.86	0.28	7.5	1.1	0.11	0.08	20	11
L249_7	4.02	0.63	-	-	1.8	1.0	15.9	5.8	210	380	13.60	0.28	5.9	1.5	0.06	0.07	6.6	0.3
L249_8	3.89	0.75	-	-	1.6	1.2	26.5	6.5	370	410	13.73	0.28	5.4	1.4	0.11	0.06	5.7	0.3
L249_9	4.70	0.62	-	-	1.7	1.2	22.1	5.3	430	350	13.00	0.31	7.7	1.3	0.18	0.09	53	14
L249_10	4.43	0.75	-	-	7.4	2.7	23.4	6.5	260	380	12.80	0.30	6.0	1.3	0.94	0.38	260	130

Sample	Mn	2SE	Co	2SE	Ni	2SE	Zn	2SE	Y	2SE	Zr	2SE	Nb	2SE
L249_1	1515	10	164	2	3768	28	174.1	5.0	0.071	0.010	-	-	0.017	0.014
L249_2	1540	11	164	2	3738	32	151.6	2.9	0.058	0.008	0.05	0.02	0.015	0.013
L249_3	1592	15	163	2	3823	44	158.5	5.5	0.077	0.010	0.97	0.15	0.005	0.015
L249_4	1656	17	162	2	3804	43	162.2	4.1	0.035	0.007	-	-	0.002	0.014
L249_5	1532	16	162	2	3806	48	161.4	4.1	0.047	0.007	-	-	-	-
L249_6	1621	8	165	2	3859	26	165.3	2.9	0.069	0.011	-	-	0.045	0.014
L249_7	1723	15	163	2	3895	27	160.7	3.5	0.074	0.011	-	-	0.022	0.014
L249_8	1613	9	165	1	3916	29	165.9	3.6	0.062	0.011	-	-	0.024	0.016
L249_9	1634	10	165	1	3865	27	163.6	3.5	0.059	0.009	-	-	0.028	0.013
L249_10	1654	20	162	2	3774	56	173.5	7.1	0.055	0.009	-	-	0.023	0.015